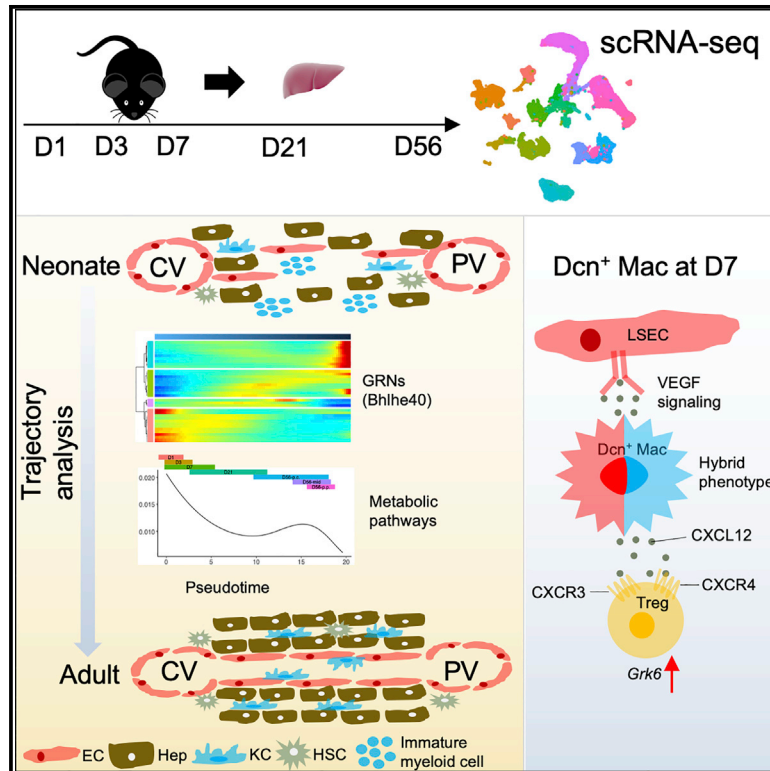


Developmental Cell

Temporal analyses of postnatal liver development and maturation by single-cell transcriptomics

Graphical abstract



Authors

Yan Liang, Kota Kaneko, Bing Xin, Jin Lee, Xin Sun, Kun Zhang, Gen-Sheng Feng

Correspondence

gfeng@health.ucsd.edu

In brief

Liang et al. presented an atlas of mouse liver development at single-cell resolution from newborn to adult. They demonstrated functional maturation of hepatocytes in concert with endothelial, stellate, and Kupffer cells and the transient emergence of a macrophage group.

Highlights

- Single-cell transcriptomics of all hepatic cell types in neonatal and adult livers
- Concerted development of zoned metabolic functions in hepatocytes and NPCs
- Transient emergence of a distinct group of macrophages at postnatal day 7
- Hepatic cell-cell communications in programming postnatal liver development



Resource

Temporal analyses of postnatal liver development and maturation by single-cell transcriptomics

Yan Liang,¹ Kota Kaneko,¹ Bing Xin,¹ Jin Lee,¹ Xin Sun,² Kun Zhang,³ and Gen-Sheng Feng^{1,4,*}¹Department of Pathology, Division of Biological Sciences, and Moores Cancer Center, University of California, San Diego, La Jolla, CA 92093, USA²Department of Pediatrics, University of California, San Diego, La Jolla, CA 92093, USA³Department of Bioengineering, University of California, San Diego, La Jolla, CA 92093, USA⁴Lead contact*Correspondence: gfeng@health.ucsd.edu<https://doi.org/10.1016/j.devcel.2022.01.004>

SUMMARY

The postnatal development and maturation of the liver, the major metabolic organ, are inadequately understood. We have analyzed 52,834 single-cell transcriptomes and identified 31 cell types or states in mouse livers at postnatal days 1, 3, 7, 21, and 56. We observe unexpectedly high levels of hepatocyte heterogeneity in the developing liver and the progressive construction of the zoned metabolic functions from pericentral to periportal hepatocytes, which is orchestrated with the development of sinusoid endothelial, stellate, and Kupffer cells. Trajectory and gene regulatory analyses capture 36 transcription factors, including a circadian regulator, *Bhlhe40*, in programming liver development. Remarkably, we identified a special group of macrophages enriched at day 7 with a hybrid phenotype of macrophages and endothelial cells, which may regulate sinusoidal construction and Treg-cell function. This study provides a comprehensive atlas that covers all hepatic cell types and is instrumental for further dissection of liver development, metabolism, and disease.

INTRODUCTION

The liver executes vital functions, including metabolism, detoxification, bile secretion, and the production of plasma proteins. Hepatocytes are the main parenchymal cells, accounting for 80% of the liver volume and carrying out most of the metabolic and synthetic functions (Miyajima et al., 2014). In the adult liver, the basic architectural unit is the zoned liver lobule, in which the portal vein (PV), hepatic artery, and bile duct form a portal triad in the corner of hexagonal lobules, with the central vein (CV) in the lobule center. The blood enters the lobules from the PV and hepatic artery and exchanges nutrients and oxygen with hepatocytes while flowing through sinusoids. The hepatocyte heterogeneity along with gradients of oxygen, nutrients, and hormones, forms metabolic zones between the CV and PV areas (Jungermann and Kietzmann, 1996). Hepatocytes located in different layers along the lobule axis express different receptors, translocators, and enzymes.

Liver development is initiated around E8.5–E9.0 in mouse embryos by outgrowth of the primary liver bud from the ventral wall of the foregut (Zaret, 2002; Zhao and Duncan, 2005), driven by concerted activities of fibroblast growth factors (FGFs) from the adjacent cardiac mesoderm and bone morphogenetic proteins (BMPs) from septum transversum mesenchyme (STM). By E9.5, the parenchymal progenitor cells delaminate from the bud and invade the surrounding STM as cords of hepatoblasts that can differentiate into hepatocytes and cholangiocytes, the biliary epithelium. Subsequent liver organogenesis that generates the complex architecture involves extensive differentiation

of parenchymal and nonparenchymal cell (NPC) types, development of the biliary tract, sinusoidal capillaries, and vasculature, and organization of extracellular matrix. Remarkably, the fetal liver is the main site of hematopoiesis, harboring hematopoietic stem cells from E10.5 to E16.5 (Crawford et al., 2010; Sasaki and Matsumura, 1986). During the late stage of embryogenesis, the liver transitions to a primary organ of metabolism, following the migration of hematopoietic stem cells to the bone marrow (Gordillo et al., 2015; Zaret, 2002).

Single-cell RNA sequencing (scRNA-seq) has been used to characterize the landscape of the mouse gut endoderm and gastrulation (Nowotschin et al., 2019; Pijuan-Sala et al., 2019) and to dissect differentiation of the bipotential hepatoblasts into hepatocyte and cholangiocyte lineages (Yang et al., 2017). A comprehensive scRNA-seq analysis characterized the onset of liver development from the specification of endoderm progenitors to parenchymal and nonparenchymal cell-lineage diversification and establishment in E7.5–E10.5 mouse embryos (Lotto et al., 2020). Another study investigated single-cell transcriptomes in endodermal and hepatic cells from E7.5 to E15.5 in Foxa2^{eGFP} mouse line (Mu et al., 2020).

After birth, hepatocytes organize into hepatic lobules, establishing the zonation structure. However, the driving factors of zonal construction and how hepatocytes adopt specific metabolic functions remain to be determined. One microarray analysis demonstrated four developmental stages from E11.5 to normal adult liver with distinct transcriptome profiles (Li et al., 2009). The dividing points of four stages are E14.5, E17.5, and day 3. Another study using bulk RNA-seq focused



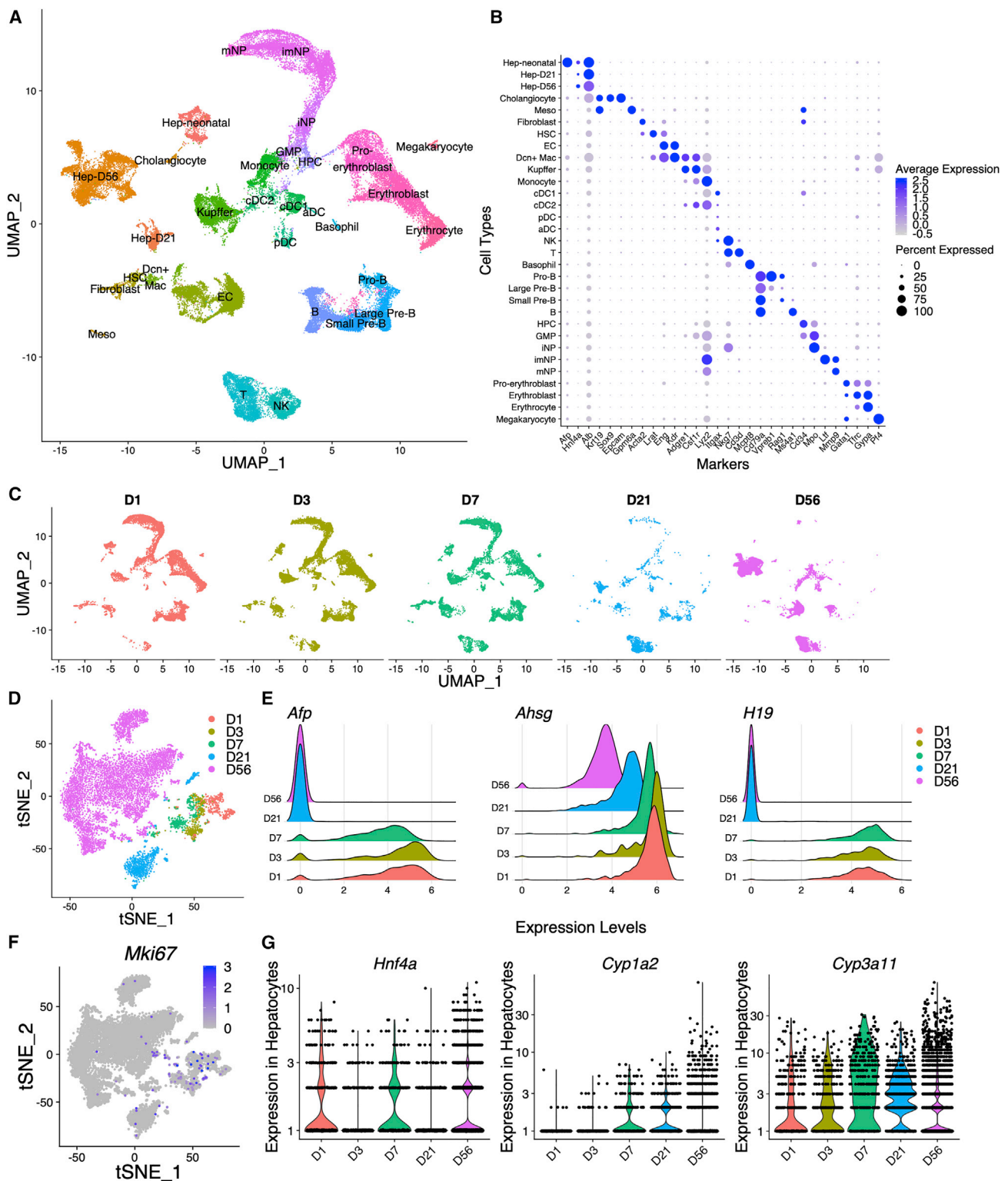


Figure 1. scRNA-seq identifies hepatic cell types in the developing and adult liver

(A) UMAP visualization of liver cell types at D1, D3, D7, D21, and D56. Colors indicate cell types, including hepatocyte (Hep-neonatal from D1, D3, and D7; Hep-D21; Hep-D56), endothelial cell (EC), hepatic stellate cell (HSC), cholangiocyte, fibroblast, mesothelial cell (Meso), megakaryocyte, erythroid cell (pro-erythroblast, erythroblast, and erythrocyte), T cell, natural killer (NK) cell, B cell (Pro-B, large pre-B, small pre-B, and B), dendritic cell (classical dendritic cell 1 – cDC1, classical dendritic cell 2 – cDC2, plasmacytoid dendritic cell – pDC, and activating dendritic cell – aDC), monocyte, *Dcn*⁺ macrophage (*Dcn*⁺ Mac), Kupffer cell,

(legend continued on next page)

more on postnatal development from E17.5 to day 60 (Gunewardena et al., 2015). However, the bulk data analyses provided only the average values of different cell types, thus confounding the critical information on changes in cell-type composition, cell-cell interaction, and functional heterogeneity. Combined use of scRNA-seq with single-molecule fluorescence *in situ* hybridization allowed reconstruction of liver zonation and inference of lobule coordinates in fasted adult mice, with more than half of the liver genes shown to be significantly zoned, albeit the analysis was focused on hepatocytes only (Halpern et al., 2017).

In this study, we isolated all major hepatic cell types for comprehensive analysis of progressive liver development in mice after birth at single-cell resolution. We revealed the process of hepatocytes and sinusoidal endothelial cell (EC) zonation establishment and identified candidate regulators in hepatocyte development and their putative roles in tumorigenesis. We performed computational predictions of the circadian rhythm development in the liver as well as response of several critical metabolic pathways in hepatocytes after birth, including glycolysis, fatty-acid β -oxidation, and lipid and cholesterol biosynthesis. Remarkably, we identified a special group of macrophages, enriched on postnatal day 7 and inferred their role in regulating sinusoidal vascularization and regulatory T (Treg) cell activity via cell-cell communication analysis. Herein, we present a detailed single-cell atlas of postnatal liver development.

RESULTS

scRNA-seq identifies distinct hepatocyte subpopulations in the early postnatal liver

To investigate liver development at single-cell resolution, we established a protocol for efficient isolation of all hepatic cell types, including hepatocytes and nonparenchymal cells (NPCs), from the mouse liver at high quality (see STAR Methods). We collected cells at postnatal days 1, 3, 7, 21, and 56 (marked as D1, D3, D7, D21, and D56), which cover the whole period of liver development from newborn to adult. All isolated single cells were used for scRNA-seq on a 10x Genomics platform (Table S1; Figure S1A). Of a total of 65,891 cells subjected to RNA-seq, 52,834 cells passed quality control based on the number of genes expressed, the count of raw reads, and the mitochondrial gene percentage. Cells from the five time points were normalized and scaled for clustering and dimensional reduction using UMAP (Figures 1A and 1C). We identified a total of 31 cell types or states from all ages, based on expression of manually selected well-known markers (Figure 1B; Table S2). Within the 31 clusters, we identified three groups of hepatocytes (Figure 1A). Hep-neonatal consisted of hepatocytes collected at the early stages,

including D1, D3, and D7, whereas Hep-D21 and Hep-D56 included hepatocytes at D21 and D56, respectively.

We investigated 9,137 assigned hepatocytes from D1 to D56, expressing the biomarkers *Alb* and *Hnf4a* (Figure 1B). These cells were clustered primarily by time points (Figure 1D), with hepatocytes from D1, D3, and D7 located closer, relative to the D21 and D56 cells. Several hepatoblast or hepatocellular carcinoma (HCC) markers, such as *Afp*, *Ahsg*, and *H19* (Spear et al., 2006; Su et al., 2017), were highly expressed by hepatocytes at the early time points (Figure 1E), suggesting that they are not mature hepatocytes. Indeed, hepatocytes at D1-D7 were actively proliferating, with high expression of *Mki67*, encoding the proliferation marker Ki67 (Figure 1F), as well as other markers of proliferation (Whitfield et al., 2006), including *Mybl2*, *Top2a*, and *Ccnd1* (Figure S1B). Hepatocytes from D21 were at a transition status, with low expressions of *Mki67*, *Afp*, *Ahsg*, and *H19* (Figures 1E and 1F) and also low levels of *Hnf4a*, *Cyp1a2*, and *Cyp3a11* (Figure 1G), mature hepatocyte markers in adult liver (D56).

At each time point, we identified 2–3 subgroups (Figures 2A–2E), with a few marker genes shared at multiple time points. D1-Hep1, D3-Hep1, and D7-Hep1 highly expressed *Rpl10*, *Fabp5*, and other ribosomal proteins, suggesting active protein translation. D1-Hep2, D3-Hep2, and D7-Hep2 highly expressed metabolism-related genes, *Cyp4a14* and *Cps1* (Figures 2A–2C and S1C). At later stages, D21-Hep2 and D56-Hep2 highly expressed *Neat1*, *Mlxipl*, and *Malat1*; D21-Hep3 and D56-Hep3 expressed *Snca* and *Cd24a* (Figures 2D, 2E, and S2A). Interestingly, D1-Hep3 was featured by unique expression of *Scd2* (Figures 2F and S1C), encoding an isoform of stearoyl-CoA desaturase (SCD)—a key enzyme for biosynthesis of mono-unsaturated fatty acids (Miyazaki et al., 2003, 2005). *Scd1* expression was abundant at D21 and D56, whereas *Scd2* was mainly expressed at D1 (Figures 2G, 2H, S1D, and S1E). We validated the distinct *Scd1* and *Scd2* expression patterns in isolated hepatocytes by qRT-PCR (Figures 2I–2J and S1L). Similar age-related expression profiles of *Scd1* and *Scd2* were observed in hepatic stellate cells (HSCs) (Figures S1F and S1G) and Kupffer cells (Figures S1H and S1I), as validated by qRT-PCR in isolated Kupffer cells (Figures S1J–S1L). *Scd2* expression peaked in Kupffer cells at D7 (Figure S1I), similarly detected by qRT-PCR (Figure S1K).

We identified two rare hepatocyte subgroups at D21 and D56 (Figures 2D and 2E). Cells in Hep3 highly expressed *Cd24a* (Figure S2A), a hepatoblast marker (Ochsner et al., 2007) and hepatocyte progenitors in the adult liver (Qiu et al., 2011). *Cd24a* expression was scattered in all subpopulations at neonatal stages but was constrained in Hep3 at D21 (Figure S2B). Hep2 cells were featured by high expressions of *Neat1*, *Malat1*, and *Mlxipl* (Figure S2A). *Neat1* and *Malat1* represent the most

neutrophils (immature neutrophil – iNP, intermediate mature neutrophil – imNP, and mature neutrophil – mNP), basophil, granulocyte-monocyte progenitor (GMP), and hematopoietic progenitor cell (HPC).

(B) Expression of selected markers for cell types. The dot size corresponds to the ratio of cells expressing the gene in the cell type. The color scales correspond to the averaged expression levels. See also Table S2.

(C) Temporal UMAP visualization of hepatic cells from (A). The UMAP was separated and colored by time points ($n = 2-4$ for each time point).

(D) tSNE map of hepatocytes from 5 time points (indicated by 5 colors). Cells in Hep-neonatal, Hep-D21, and Hep-D56 from (A) were segregated and reanalyzed.

(E) Ridge plots displaying the expression distributions of indicated markers in hepatocytes from (D) at 5 time points. x axis indicates log-normalized expression levels.

(F) tSNE map displaying *Mki67* expression in hepatocytes from (D).

(G) Violin plots displaying expression levels of indicated markers in hepatocytes from (D). The y axis indicates log-normalized expression levels.

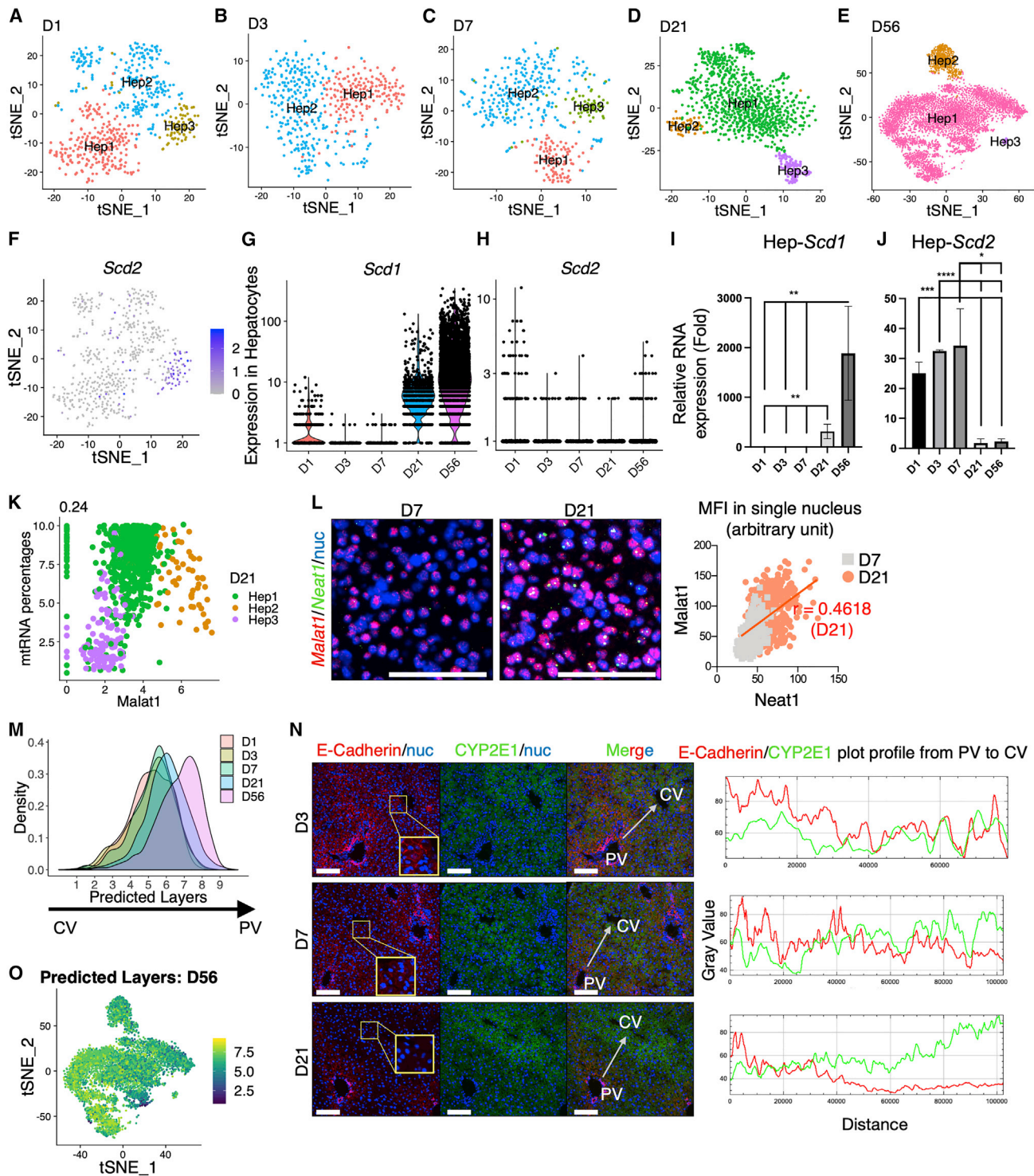


Figure 2. scRNA-seq identifies distinct transcriptome profiles in hepatocytes at each time point

(A–E) tSNE map of hepatocytes from D1 (A), D3 (B), D7 (C), D21 (D), and D56 (E). Colors indicate subpopulations identified.

(F) tSNE map displaying *Scd2* expression in D1 hepatocytes from (A).

(G and H) Violin plots displaying *Scd1* (G) and *Scd2* (H) expression in hepatocytes. y axis indicates log-normalized expression.

(I and J) qRT-PCR analysis of *Scd1* (I) and *Scd2* (J) expression in isolated hepatocytes. Statistical analysis used Student's t test. Values are presented as means \pm SD. (***) $p < 0.001$, (**) $p < 0.01$, (*) $p < 0.05$. See also Figure S1L for cell-type marker expression.

(legend continued on next page)

abundant lncRNAs in nuclei, and *Mlxip1* is one of the few predominantly spliced polyadenylated protein-coding mRNAs showing nuclear retention (Bahar Halpern et al., 2015). *Malat1* has been frequently detected in scRNA-seq datasets, with its expression associated with mitochondrial RNA (mtRNA) proportions and cell death (Alvarez et al., 2020). We observed a high correlation between *Malat1* expression and mtRNA proportions in Hep1 and Hep3 cells but not in Hep2 (Figure 2K), supporting a notion that Hep2 is not a group of poor-quality cells. Next, we performed small molecule fluorescence *in situ* hybridization (smFISH) for *Neat1* and *Malat1* at D7 and D21 (Figure 2L). Pearson's correlation analysis showed highly correlated expressions of *Malat1* and *Neat1*, identifying a group of hepatocytes at D21 featured by their coexpression.

Progressive establishment of the zonation pattern along the lobule axis

We explored the distribution of hepatocytes in a lobule by examining expression of four zonation markers, *Cyp2f2*, *Cyp2e1*, *Cdh1*, and *Glul* (Figure S2C) (Braeuning et al., 2006). As reported earlier (Doi et al., 2007; Halpern et al., 2017), *Cyp2e1* was most abundant in the CV area and decreased gradually toward the PV region, with *Cyp2f2* having the opposite pattern. *Glul*, encoding glutamine synthetase (GS), was only expressed in pericentral hepatocytes, whereas *Cdh1*, encoding E-cadherin, was expressed in periportal hepatocytes. The spatial location of hepatocytes at D56 was clearly visible based on the expression of these four markers, which were inexplicit at earlier time points (Figure S2C). A previous study divided hepatic lobules into nine layers based on scRNA-seq and smFISH data (Halpern et al., 2017). We trained that dataset with assigned layers and inferred a spatial location of single cells from hepatocyte clusters (see STAR Methods; Table S3). Layer 1 represents hepatocytes in the CV area, with layer 9 near PV. The predicted layer distribution at D56 (Figure 2M) was consistent with the prior probabilities of the proposed adult liver zonation model (Halpern et al., 2017), with the density peaking in layer 8. However, the predicted zonation profiles at earlier time points did not show similar patterns (Figure 2M), suggesting progressive zonal construction in the postnatal liver. The heatmaps of the 18 most significant zonation hallmark genes in hepatocytes demonstrate a gradually distinguishable CV to PV transition from D1 to D56 (Figure S2E). *Glul* expression was high in pericentral hepatocytes starting from D1, albeit with gradual restriction to the CV area, whereas percentages of PV gene-positive hepatocytes increased steadily toward D56. Consistently, immunostaining of E-cadherin and CYP2E1 showed reciprocally increasing expression in PV and CV hepatocytes, respectively (Figure 2N). A previous study reported a

similar pattern of E-cadherin and GS in hepatocytes during postnatal development (Gola et al., 2021). We mapped the predicted layers back to tSNE visualization at D21 and D56 (Figures 2O and S2D). Although immunostaining detected opposite expression patterns of E-cadherin and CYP2E1 in the CV and PV areas at D21, relative to D3 and D7 (Figure 2N), transcriptomic profiling showed that most hepatocytes from different layers were still mixed at D21 (Figure S2D), suggesting that the metabolic zones are not fully developed yet in D21 hepatocytes. Consistent with the expression of zone markers (Figure S2C), zoned hepatocytes could only be distinguished at D56 (Figure 2O).

We established developing trajectory and calculated the pseudotime for each single cell (Figures 3A and 3B) using Monocle (Qiu et al., 2017; Trapnell et al., 2014). The D56 hepatocytes were divided into three groups, D56-p.c., D56-mid, and D56-p.p., based on the predicted layer and randomly down-sampled to be comparable with other time points. Because liver samples were collected from D1 to D56, the real-time points could be used to evaluate accuracy of the pseudotime calculation (Figure 3C). At D56, the pericentral hepatocytes (D56-p.c.) showed up first in the trajectory, followed by the midlobular (D56-mid) and then the periportal (D56-p.p.). Consistently, zonation prediction also showed steady increases of periportal hepatocytes toward D56 (Figure 2M), suggesting that the periportal hepatocytes are functionally matured later.

Identification of transcription factors in programming liver development

We ordered single hepatocytes from all time points by pseudotime and performed differential expression analysis to identify genes whose expression changed significantly as a function of pseudotime. These selected genes were then grouped into six clusters by pseudotemporal expression patterns (Figures 3D and S10; Table S4). For each cluster, we performed pathway enrichment analysis with simplified gene-set collection from Molecular Signatures Databases (MSigDB) (Subramanian et al., 2005), with the significantly enriched pathways in each cluster listed in Table S4. The peripheral circadian clock-related pathway was identified in cluster 1, where genes were gradually increased from D1 to D56.

To search for transcription factors (TFs) as developmental regulators, we performed single-cell regulatory network inference and clustering (SCENIC) (Aibar et al., 2017), which allows the construction of gene regulatory network (GRN) using the same subset of single cells for trajectory analysis. A TF activity matrix was generated with scores that measure expression levels of the TF's downstream targets (regulon) in a single cell. This approach captured 36 TFs that exhibited significant changes as a function

(K) Scatter plot displaying correlation between *Malat1* expression (x axis) and mtRNA percentage (y axis). Pearson correlation coefficient (0.24) is shown above the plot. *Malat1* expression is log-normalized value. mtRNA percentage is the proportion of transcripts mapped to mitochondrial genes. Colors indicate D21 subpopulations in (D).

(L) (Left) smFISH of *Malat1* and *Neat1* at D7 and D21. (Right) The quantitative results showing fluorescence signal intensity (MFI) and correlation coefficient between *Malat1* and *Neat1*. Scale bar, 100 μ m.

(M) Density plot displaying distribution of predicted layers of hepatocytes. The predicted layer for each hepatocyte was normalized from layer 1 (CV area) to layer 9 (PV area). See also Table S3 for gene signatures used for zonation prediction.

(N) (Left) Immunostaining of E-cadherin and CYP2E1 in D3, D7, and D21 livers. Scale bar, 100 μ m. The insets show loss of E-Cad around CV over time, establishing a clear zonation. (Right) Quantitative results showing the changing expression levels from PV to CV as the arrow indicates.

(O) tSNE map displaying predicted layers for D56 hepatocytes from (E). Color bar indicates predicted layers from layer 1 (CV area) to layer 9 (PV area).

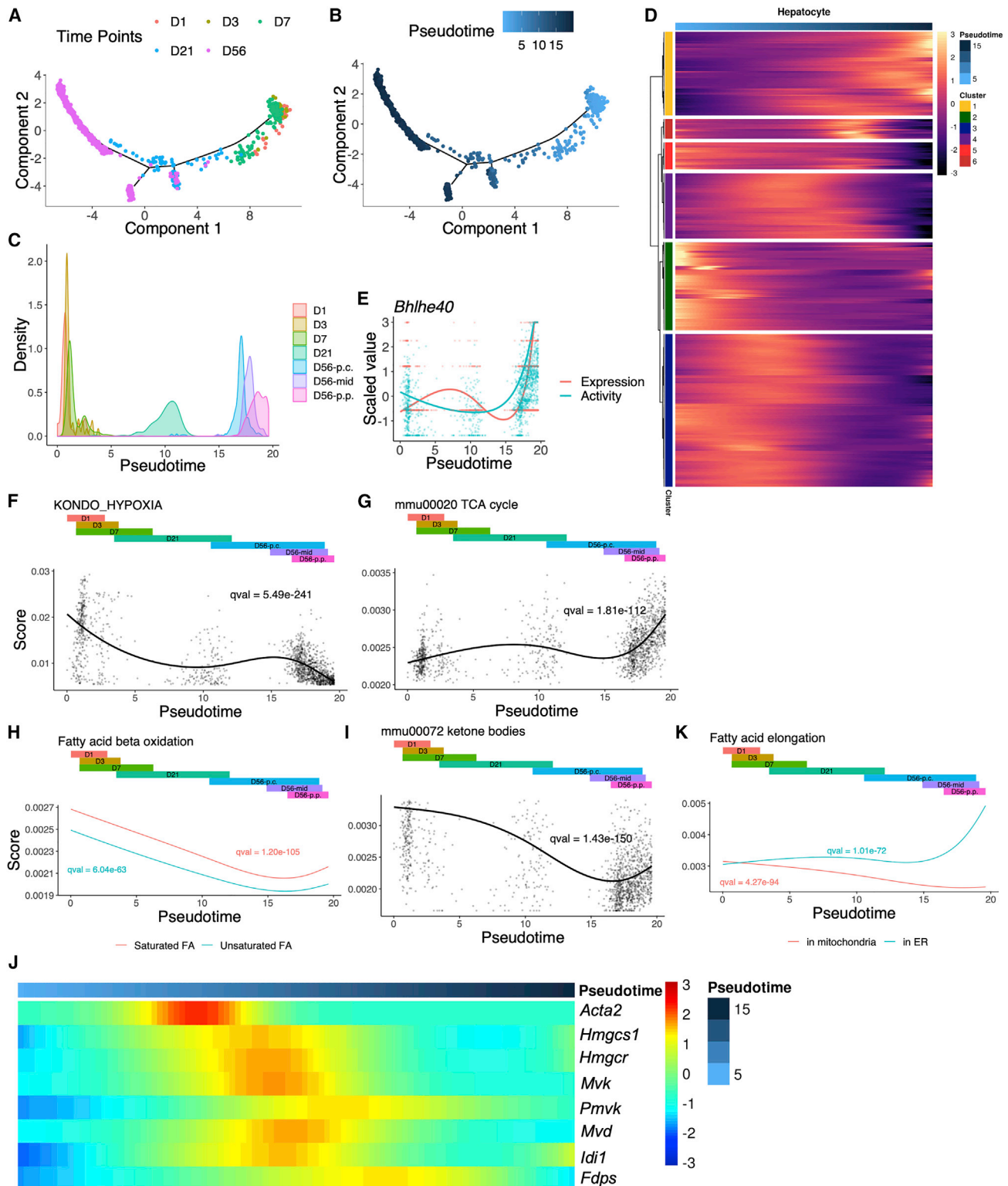


Figure 3. Dynamic changes of transcription factor activities and metabolic functions in hepatocytes

(A) Pseudotime analysis of hepatocyte development from D1 to D56 with Monocle.
 (B) Pseudotime analysis of data in (A). Color indicates inferred pseudotime used for (C)–(K).
 (C) Density plot displaying distribution of inferred pseudotime (x axis).

(legend continued on next page)

of pseudotime in both expression and activity (Figures S3A and S3B), including *Bhlhe40* (Dec1)—a core regulator of circadian rhythm (Honma et al., 2002; Sato et al., 2004). Its expression and activity increased dramatically at the later stage (Figure 3E), consistent with the pathway enrichment data (Figure 3D; Table S4).

Among the 36 TFs, *Jun*, *Junb*, and *Fos* are known to play important roles in tumorigenesis, and we explored the other TFs in HCC. During postnatal development, *Klf9* showed steadily increasing expression and activity after birth, whereas an opposite pattern was observed for *Hmgb2*, with the highest level detected at the onset (Figure S3C). RNA-seq data analysis of 371 patients with HCC deposited in TCGA demonstrated that patients with higher *Klf9* expression and activity had longer survival (Figures S3D and S3E), with the activity scores steadily decreasing with tumor progression (Figure S3F). In contrast, we observed shorter survival for patients with high *Hmgb2* expression and activity, which also exhibited an increasing trend with disease progression (Figures S3D and S3E). Thus, patients with higher expression and activity of a TF active in the early postnatal stage showed poorer prognosis.

Development of various metabolic functions in hepatocytes

To explore the development of metabolic functions in hepatocytes, we calculated the pathway enrichment scores of gene sets collected from the Kyoto Encyclopedia of Genes and Genomes (KEGG) database (Kanehisa and Goto, 2000) and MSigDB (Subramanian et al., 2005). We then ordered cells along pseudotime and filtered for gene sets whose scores significantly changed along the trajectory. Furthermore, we visualized gene sets of interest through fitting a natural spline (see STAR Methods) and investigated the detailed changes of genes in each gene set. Hepatocytes use glycolysis as the main energy source in the fetus because of low oxygen and under-developed mitochondria. The metabolic energy source shifts in the newborn because of the rapid increase in mitochondrial oxidative phosphorylation with air breathing (Böhme et al., 1983; Lindgren et al., 2019). We observed steadily decreasing expression of hypoxia-related pathway from D1 to D56 (Figure 3F). The hypoxia pathway was more prominently suppressed in the PV than in the CV area at D56, with an opposite pattern observed for the tricarboxylic acid (TCA) cycle (Figure 3G). Expression of most glycolysis-specific genes slowly increased when the glucose level restored and decreased subsequently, whereas gluconeogenesis-specific genes, including *Pcx* and *Fbp1*, were highly expressed right after birth (Figure S4A). This observation was consistent with sudden hypoglycemia at birth because of disruption of glucose supply from mothers (Böhme et al., 1983), which could be remedied by enhanced gluconeogenesis. Similarly, glycogenolysis-specific genes also peaked at early stages (Fig-

ure S4B) to replenish blood glucose, although glycogenesis showed up later and peaked in periportal hepatocytes at D56.

We observed a peak of fatty-acid β -oxidation immediately after birth, followed by a rapid decrease over time and slight increase in periportal hepatocytes at D56 (Figure 3H), producing large amounts of acetyl-CoA. A ketone body-related pathway showed a similar pattern as β -oxidation, with a peak right after birth (Figure 3I). The genes involved in mevalonate pathway for cholesterol biosynthesis were modestly expressed in newborns but peaked at D21 (Figure 3J), suggesting that the pathway is not well established in neonatal livers. Short fatty-acid elongation in mitochondria might be important for hepatocytes in the newborn liver, although ER dominated this process later during development (Figure 3K). Bile secretion peaked in the PV region at D56 (Figure S4C), and enzymes in urea production from ammonia, encoded by *Cps1*, *Otc*, *Ass1*, *Asl*, and *Arg1*, increased after birth and peaked in the PV region at D56 (Figure S4D). However, metabolism of xenobiotics showed an opposing pattern (Figure S4E), with the pathway-related genes highly expressed in pericentral hepatocytes and decreased gradually in the mid-lobe and PV regions.

Development of liver endothelial and mesenchymal cells

Liver ECs consist of macrovascular endothelial cells (MaVECs), lymphatic endothelial cells, and liver sinusoid endothelial cells (LSECs). Liver ECs across all five time points were clustered into 11 subpopulations (Figure 4A), with non-LSECs sharing similar transcriptomes over time. LSECs at D56 constituted two large and continuous groups, periportal and pericentral LSECs (EC1 and EC2) (Figures 4B and S5C). In contrast, we observed higher heterogeneity in premature LSECs (EC3–EC6), without clear zonation separation. A small group of EC9 cells that expressed proliferation and cell-cycle-related genes were detected at all time points, albeit with a decreasing trend (Figure 4B). All EC9 cells were in the G2/M or S phase as predicted by cell-cycle marker genes (Figure S5D), suggesting that a pool of LSECs with proliferation potential is maintained in developing liver. MaVECs highly expressed the marker gene *Vwf* but were negative for LSEC markers *Stab2* and *Lyve1* (Géraud et al., 2010) (Figure S5A); these cells were further divided into two subtypes based on their physical location. Central vein vascular endothelial cells (CVECs), labeled as EC11, expressed CV markers *Rspo3* and *Wnt2*, and EC7, portal vein vascular endothelial cells (PVECs), expressed PV markers *Dll4* and *Efnb2* (Figure S5B) (Halpern et al., 2018). These markers effectively distinguished zonation patterns for both LSECs and MaVECs. The lymphatic ECs (EC10) expressed *Thy1* (Jurisic et al., 2010) and also *Stab2* and *Lyve1* (Figure S5A).

Previous single-cell analysis of the embryonic liver from E7.5 to E10.5 (Lotto et al., 2020) showed a developmental trajectory from hemangioblasts to embryonic endothelial cells. By combining the embryonic with our neonatal endothelial cell

(D) Heatmap representing trends of differentially expressed genes as a function of inferred pseudotime. Genes in row are grouped into 6 clusters based on expression patterns. See also Figure S10 and Table S4 for the gene list and enriched pathways.

(E) Scatter and fitted plots of *Bhlhe40* scaled expression and activity values along pseudotime. The inferred pseudotime was stretched from 0 to 100.

(F–I) Scatter plot and fitted plots of enrichment scores for indicated pathways along inferred pseudotime. Only fitted plots are shown for (H) and (K).

(J) Heatmap displaying genes from the mevalonate pathway with differential expression along inferred pseudotime.

(K) Fitted plots of enrichment scores for indicated pathway along inferred pseudotime.

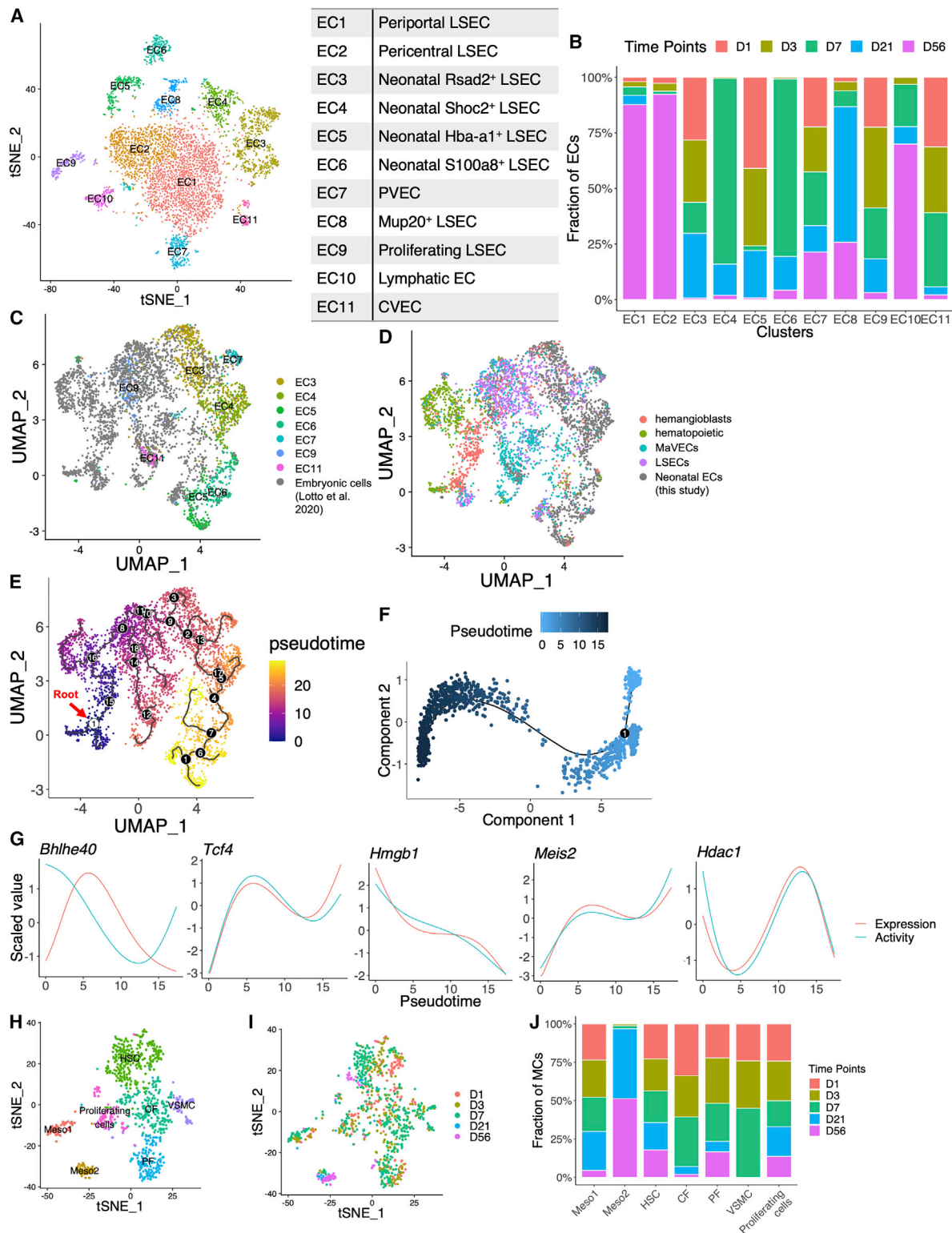


Figure 4. Development of liver endothelial and mesenchymal cells

(A) tSNE map of endothelial cells from D1 to D56. Cells in EC from Figure 1A were segregated and reanalyzed.

(B) Time point compositions of each EC subpopulation labeled in (A).

(C and D) UMAP visualization of cells from D1, D3, D7, and embryonic cells (including hemangioblasts, hematopoietic cells, HSEC, and endothelium) from published data (Lotto et al., 2020). Colors indicate endothelial cell subpopulation labeled in (A) (C) or embryonic cell types (D).

(legend continued on next page)

data (Figures 4C, 4D, and S5E), we constructed a trajectory from E7.5 to D7 (Figure 4E). The hemangioblasts with highest differentiation potential were defined as the root cells. Starting from the root, hemangioblasts differentiated into hematopoietic or endothelial cells at branch point 16. These early endothelial cells further differentiated into LSECs or MaVECs at branch point 8. Around this branching point, proliferating LSECs (EC9), which emerged after birth, exhibited similar transcriptomic profiles as early embryonic endothelial cells. Within the LSEC branch, neonatal cells developed from EC3, EC4 to EC6, and EC5. Shared the other branch with embryonic MaVECs is EC11, the neonatal CVECs. However, EC7 emerged later, consisting of neonatal PVECs, likely differentiated from EC3, the earliest subtype of neonatal LSECs. These analyses suggest that endothelial cells in PV and CV areas take separate developmental paths and that the PV area is remodeled after birth, with concerted differentiation of hepatocytes and endothelial cells in the region.

Taking similar approaches used for hepatocytes, we constructed a developmental trajectory of LSECs and calculated pseudotime for each single cell (Figures 4F, S5F, and S5G). This approach identified differentially expressed genes as a function of pseudotime, clustered by their pseudotemporal expression patterns (Figure S5H), and with the significantly enriched pathways listed in Table S5. Among genes that decreased during postnatal development, we observed enrichment of the VEGFA–VEGFR signaling pathway. We also detected several glycolysis- and hypoxia-related pathways, showing that LSECs experienced similar metabolic changes as hepatocytes after birth. For upregulated genes, we observed a significant enrichment of interferon pathways. Several TFs, including *Bhlhe40*, *Tcf4*, *Hmgb1*, and *Meis2*, exhibited significant changes in expression and activity along the LSEC developmental trajectory (Figure 4G). These TFs are possible regulators of sinusoidal buildup, of which *Meis2* was mainly expressed in endothelial cells (Figure S5I). The expression of *Hdac1*, encoding a histone deacetylase, was also remarkably changed in the process (Figure 4G). Interestingly, the circadian regulator *Bhlhe40* showed opposite expression patterns between LSECs and hepatocytes (Figure 3E).

Mesenchymal cells have been reported as the source of myofibroblasts after liver injury, especially HSCs (Iwaisako et al., 2014). We identified three main clusters of mesenchymal cells (Figure 1A), including HSCs, fibroblasts, and mesothelial cells (Meso). By segregating these cells, we identified more mesenchymal cell subgroups (Figure 4H), which were initially included within other mesenchymal cells. Two subgroups, Meso1 and Meso2 (Figure 4H), shared mesothelial markers *Gpm6a* (Li et al., 2013), *Upk3b*, and *Wt1* (Figure S5J), albeit with distinct transcriptome profiles. *Alcam*, a marker of embryonic mesothelial cells in the mouse liver (Li et al., 2013), was expressed in Meso1, but not Meso2. Of note, Meso1 was mainly constituted

by cells at the neonatal stage (Figures 4I and 4J). A previous lineage tracing experiment showed that these mesothelial cells migrated inward from liver surface and differentiated into HSCs, fibroblasts, and vascular smooth muscle cells (VSMCs) during liver development (Asahina et al., 2011). Meso2 cells expressed *Igfbp4*, *Cd34*, and *Clec3b* and emerged later at D21 and D56, in replacement of Meso1. In addition, we detected two fibroblast clusters, capsular fibroblast (CF), located beneath the liver surface, and portal fibroblast (PF), near the portal triad (Balog et al., 2020). A group of cells with proliferating potential was also identified (Figure S5K), which expressed HSC markers, *Reln* and *Lrat*, or PF markers, *Cd34* and *Clec3b* (Dobie et al., 2019) (Figure S5J).

Dynamic changes of hematopoietic and immune cell populations

Our dataset from D1 to D56 showed many clusters of developing hematopoietic cells, including hematopoietic progenitor cells (HPCs), granulocyte-monocyte progenitors (GMPs), B cells, neutrophils, and erythroid lineages (Figure 1A). Both HPCs and GMPs expressed *Cd34*, a hematopoietic precursor marker (Figure 1B). The development trajectories of these cell types were inferred by force-directed graph (FDG) analysis (Figure 5A), which corroborated the predicted relationships shown in UMAP visualization (Figure 1A). HPCs were connected to three main paths, developing toward GMPs, erythroid lineage, and B cells. GMPs then gave rise to monocytes and neutrophils. Based on markers used previously (Bjerrgaard et al., 2003; Borregaard and Cowland, 1997), neutrophil lineages exhibited three major stages: (1) immature neutrophils (iNP; or neutrophilic promyelocytes), expressing high levels of *Mpo* and *Elane* (encoding elastase); (2) intermediate mature neutrophils (imNP; or neutrophilic myelocytes and metamyelocytes), expressing *Ltf* (encoding lactoferrin); and (3) mature neutrophils (mNP) (Figure 1B). Of note, this neutrophil lineage was not detected in a recent scRNA-seq study of the human fetal liver (Popescu et al., 2019). Similarly, B cell lineage was divided into several stages. First, the immunoglobulin heavy chain gene arrangement occurred in pro-B cells with a surrogate light chain expressed. This process requires expression of *Rag1/2* for gene rearrangement and *VpreB* for the surrogate light chain (Figure 1B). A light chain rearrangement occurred in small pre-B cells expressing *Rag1/2*. Gene rearrangement, and the expression of *Rag1/2*, stopped in a middle stage, called large pre-B cells. Based on reported markers (Elliott and Sinclair, 2012), we divided the erythroid lineage into three stages, which shared similar features of hematopoiesis in adult bone marrow. Hepatic hematopoiesis persisted after birth but receded rapidly, barely detectable after D7 (Figures 5B and S6A–S6D). The development of T cell and NK cell lineages was not observed in the postnatal liver. It was reported previously (Rugh, 1990) that T cell development in the liver occurred much earlier than B cells, with T cell

(E) Pseudotime analysis of cells from (C) with Monocle 3. Root cells are labeled in white circle 1; branch points are labeled in black circles with numbers.

(F) Pseudotime analysis of ECs from D1 to D56 with Monocle. Color indicates inferred pseudotime.

(G) Fitted plot of scaled expression and activity values along pseudotime of indicated genes. The inferred pseudotime from (F) was stretched from 0 to 100.

(H) tSNE map of mesenchymal cells from D1 to D56. Cells in Meso, HSC, and fibroblast from Figure 1A were segregated and reanalyzed. Colors indicate cell types assigned.

(I) tSNE map of mesenchymal cells from (H).

(J) Time point compositions of each cell type labeled in (H).

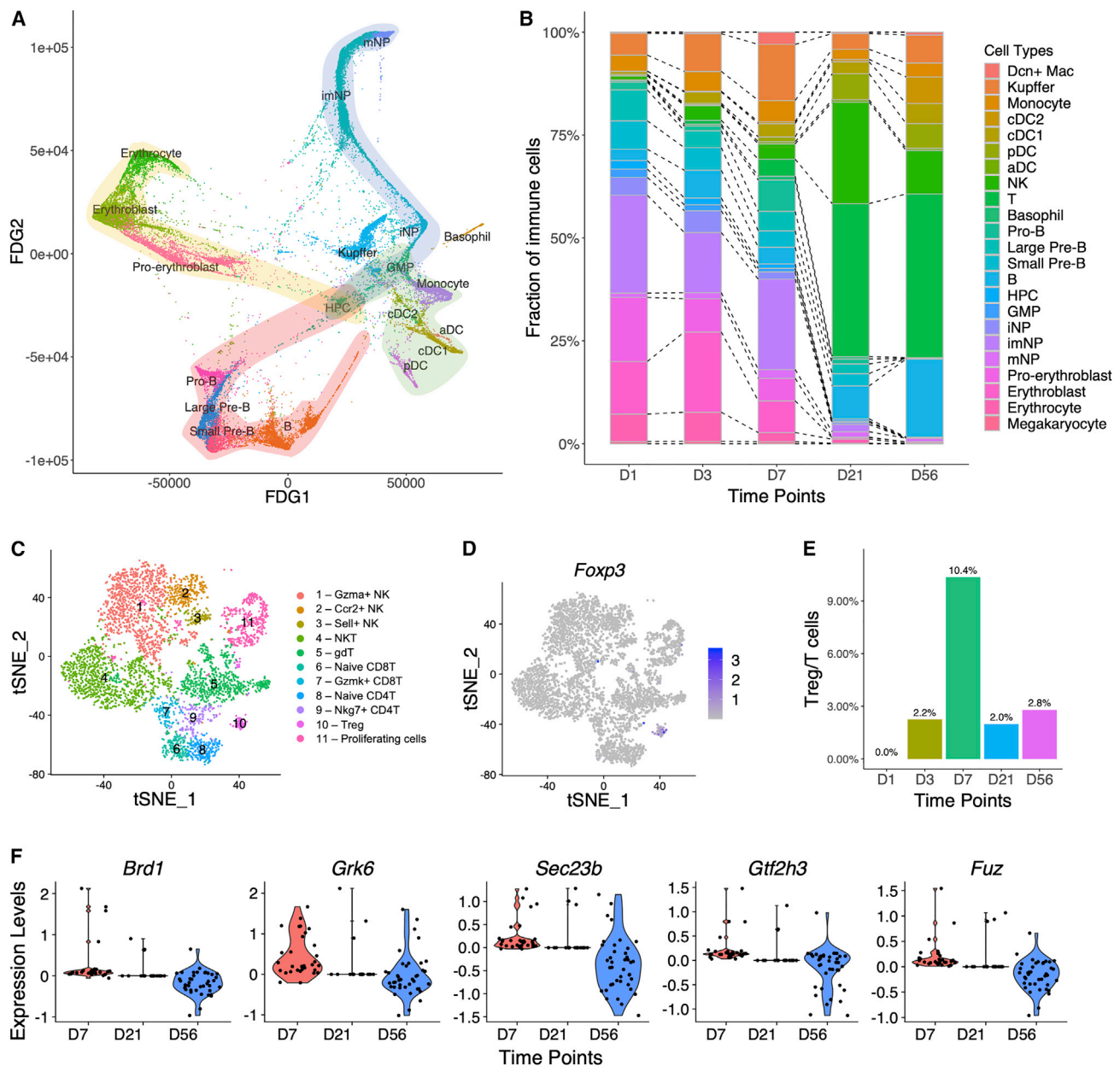


Figure 5. Dynamic changes of hematopoietic and immune cell populations

(A) Force-directed graph (FDG) of HPCs, GMPs, erythroid cells, neutrophils, B cells, DCs, basophils, monocytes, and Kupffer cells.

(B) Cell-type compositions of immune cells at each time point.

(C) tSNE map of T and NK cells from D1 to D56. Cells in T and NK clusters from Figure 1A were segregated and reanalyzed.

(D) tSNE map displaying *Foxp3* expression in cells from (C).

(E) Percentages of Treg cells out of all T cells at indicated time point.

(F) Violin plots displaying differentially expressed genes in Treg cells at D7, D21, and D56.

progenitors migrating to thymus around E13. The percentages of T and NK cells as well as dendritic cells (DCs) gradually increased over time (Figures S6E and S6F), suggesting their hepatic recruitment from thymus or bone marrow after birth.

Because of their high levels of heterogeneity, the observed changes in percentages of T or natural killer (NK) cells from D1 to D56 (Figure S6E) might not depict the patterns for individual subtypes. Thus, we segregated these cells and analyzed them

separately. Within the eleven T and NK cell subtypes identified (Figures 5C and S6G), Treg cells (Figure 5D) displayed a unique change over time, with a peak at D7 (Figures 5E and S6H). Consistently, a recent report (Li et al., 2020) showed hepatic accumulation of Treg cells between D7 and D14 after birth. We compared differentially expressed genes in Treg cells between D7, D21, and D56. Among the top-ranked genes were *Brd1* and *Gtf2h3* (Figure 5F), likely involved in cell proliferation

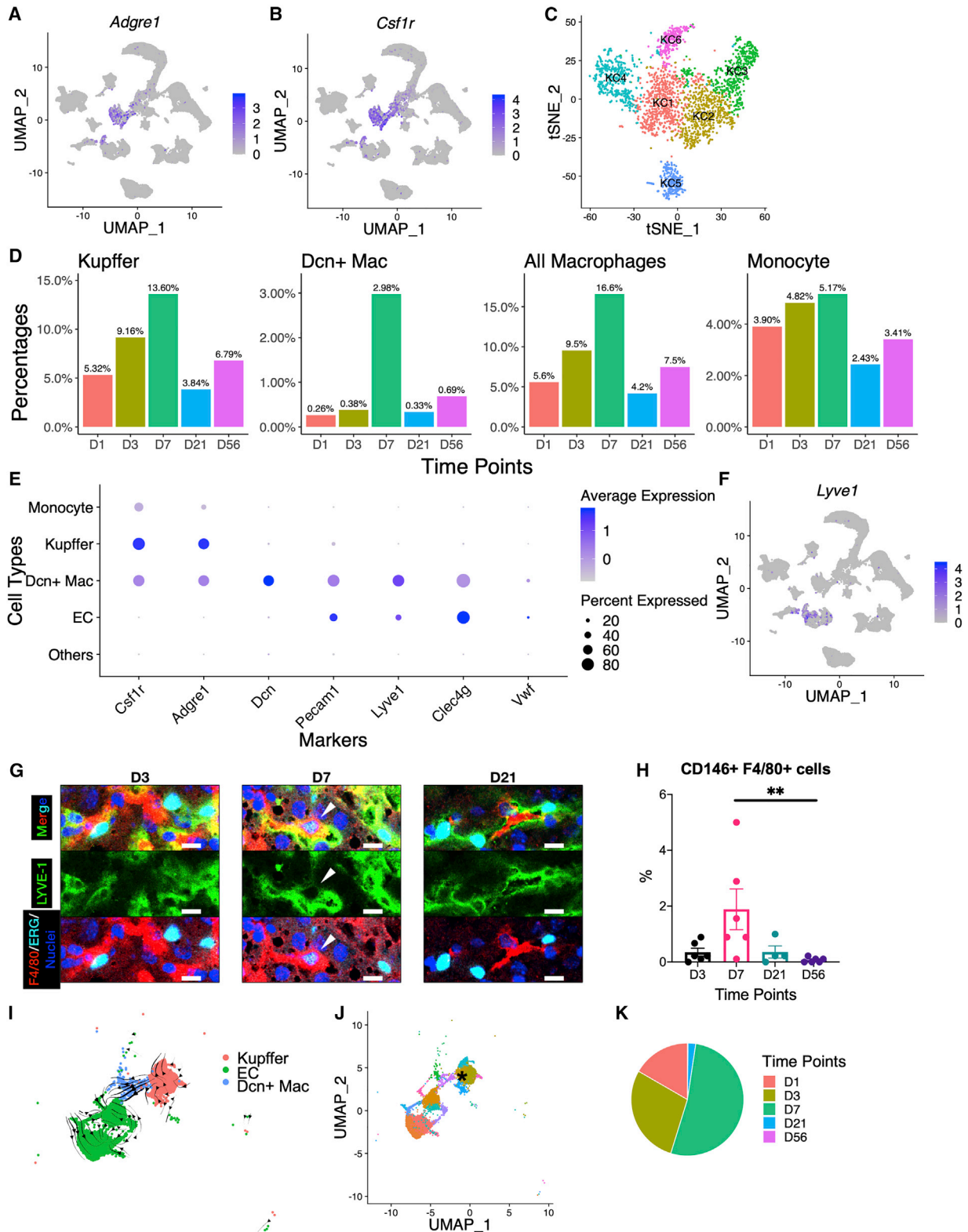


Figure 6. A subtype of macrophages emerges transiently around postnatal day 7

(A and B) UMAP visualization of *Adgre1* (A) and *Csf1r* (B) expression levels in all cells included (Figure 1A).

(C) tSNE map of Kupffer cells from D1 to D56. Cells in Kupffer clusters from Figure 1A were segregated and reanalyzed.

(D) Percentages of indicated cell types out of total immune cell population.

(legend continued on next page)

(Drapkin et al., 1996; Mishima et al., 2011; Mishima et al., 2014). Treg cells also highly expressed *Grk6*, encoding a G-protein-coupled receptor kinase that phosphorylates CXCR4 upon CXCL12 binding (Busillo et al., 2010).

A unique subtype of macrophages emerges transiently around postnatal day 7

A Kupffer cell cluster was located close to dendritic cells (DCs) and monocytes on UMAP (Figure 1A). This cluster expressed Kupffer cell markers *Adgre1* (encoding F4/80) and *Csf1r* (Ginhoux and Guilliams, 2016) (Figures 1B, 6A, and 6B), with a peak at D7 (Figure 6D). When analyzing Kupffer cells separately (Figures 6C, S7A, and S7B), we identified six subtypes, KC1–KC6, with distinct gene expression profiles (Figure S7C) and TF activities (Figure S7D). The KC6 group emerged at D1, with high expression of *Ccl9* and high TF activity of *Nfil3*. KC5 mainly emerged at D56, featured by *Ly6a* and *Cxcl13* expression and high TF activity of *Zbtb7a* and *Irf2*. Other subtypes (KC1–KC4) consisted of Kupffer cells from D1 to D21, with most gene expression patterns conserved over time. KC1 showed high expression of ribosomal proteins and *Myc* activity, and KC4 included actively proliferating cells.

We identified a subcluster of macrophages (*Dcn*⁺ Mac), featured by high expression of decorin (Table S2), a member of small leucine-rich proteoglycan family (Iozzo, 1999). Besides the traditional Kupffer cell markers, *Adgre1* and *Csf1r* (Figures 1B, 6A, 6B, and 6E), the *Dcn*⁺ macrophages also expressed general EC markers *Pecam1*, *Eng*, *Kdr*, and LSEC markers *Lyve1* and *Clec4g*, albeit negative for a MaVEC marker *Vwf* (Figures 1B, 6E, and 6F). Almost all the *Dcn*⁺ macrophages emerged at D7 (Figure 6D), which prompted a thorough investigation of this unique subtype. We validated the existence of *Dcn*⁺ Mac and its abundance at D7 by coimmunostaining for the LSEC marker LYVE-1, the endothelial cell-specific TF, ERG, and the macrophage marker F4/80 (Figure 6G). FACS analysis also detected this cell type and validated its peak level at D7 (Figure 6H). RNA velocity analysis showed a developmental trajectory of *Dcn*⁺ Mac from Kupffer cells rather than ECs (Figure 6I). We plotted top 10 genes significantly upregulated in *Dcn*⁺ macrophages via phage portraits (Figure S8A), which requires further validation by cell-lineage tracing. The group of Kupffer cells at the transition point (Figure 6J; transitioning KC, labeled by an asterisk) was identified at D1, D3, and D7 (Figure 6K), showing differentiation potential at the neonatal stage. Then, we mapped six Kupffer cell subpopulations in this UMAP (Figure S8B). The transitioning KCs were derived primarily from KC2 and displayed high TF activity of *Pou2f2* and *Tcf7l2* (Figure S7D), which might drive *Dcn*⁺ Mac transition from KC2. Several recent reports (Charkarov et al., 2019; Lim et al., 2018) addressed macrophages

expressing one EC marker, LYVE1. In contrast, the *Dcn*⁺ Mac detected in this study exhibited a combination of macrophage and EC gene expression profiles. To identify genes selectively expressed in transitioning KC, we performed differential gene expression analysis between the transitioning KC and other Kupffer cells located far from *Dcn*⁺ Mac (Figure 6J). Most genes highly expressed in lung LYVE1-expressing macrophages, including *Fcna*, *Marco*, *Cd163*, *Cd209f*, *Timd4*, and *Mrc1* (Charkarov et al., 2019; Lim et al., 2018), were significantly expressed in transitioning KC (Figure S8C).

By ligand-receptor analysis using CellPhoneDB (Efremova et al., 2020), we identified cell types actively interacting with *Dcn*⁺ Mac, including HSCs, fibroblasts, mesothelial cells, cholangiocytes, VSMCs, and all subtypes of ECs, with much less interactions observed between these cell types and Kupffer cells (Figures 7A and S9A). We then examined signaling cross-talk related to *Dcn*⁺ Mac, as compared with Kupffer cells (Figure 7B). To explore possible influences of *Dcn*⁺ Mac on other cell types, we focused on pairs with ligands expressed by *Dcn*⁺ Mac and receptors expressed on other cell types. This analysis detected several VEGF-related pairs between *Dcn*⁺ Mac and LSEC, none of which was identified between Kupffer cell and LSEC. *Dcn*⁺ Mac also secreted CXCL12 that binds CXCR3 and CXCR4 on Treg cells. Together with high expression of *Grk6* in Treg cells at D7 (Figure 5F), these data may be indicative of the significance of Treg accumulation at D7 (Figure 5E) and potential cross-talk between Treg and *Dcn*⁺ Mac cells.

Intercellular communications between hepatocytes and NPCs

Using the same method described above, we also investigated cross-talk between hepatocytes and NPCs and the dynamic changes in intercellular signaling at the early postnatal stages. We performed ligand-receptor analysis for all five time points individually. To investigate the cell-cell interactions that regulate hepatocyte zonation, we filtered for significant pairs with the receptors expressed on hepatocytes and previously shown to be zoned. This analysis identified RSPO1/3-LGR5 interactions between LSECs and hepatocytes (Figure 7C). RSPO3-LGR5 was significantly expressed across all time points, whereas RSPO1-LGR5 was only identified at the neonatal stage. The binding of RSPO to LGR5, present on pericentral hepatocytes, promotes Wnt signaling, which modulates zoned metabolic activities in the pericentral area (Planas-Paz et al., 2016; Rocha et al., 2015; Torre et al., 2010). This signaling event was also identified between Kupffer cells and hepatocytes across all time points (Figure 7D). We also identified ASGR2-F8 interaction between hepatocytes and LSECs. ASGR2 is a marker of periportal hepatocytes (Halpern et al., 2018). We then counted the

(E) Dot plots displaying expression levels of selected markers for indicated cell types. Dot size corresponds to the ratio of cells expressing the gene in the cell type. The color corresponds to the scaled average expression level.

(F) UMAP visualization of *Lyve1* expression levels in all cells included in this study (Figure 1A).

(G) Immunostaining of F4/80, ERG, and LYVE-1. Representative image taken under confocal microscope. *Dcn*⁺ Mac cells were indicated by white arrowhead. Scale bar, 10 μ m.

(H) Quantified FACS data of CD146⁺ F4/80⁺ cells in isolated NPCs, showing an enrichment at D7. Statistical analysis was done with Kruskal-Wallis test, followed by Dunn's test (** $p < 0.01$).

(I) RNA velocities of Kupffer cell, EC, and *Dcn*⁺ Mac from D1 to D56, visualized on UMAP.

(J) Clustering analysis of cells from (I). The Kupffer cell cluster showing differentiation potential to *Dcn*⁺ Mac was labeled by asterisk (transitioning KC).

(K) Time point composition of asterisk labeled cluster (transitioning KC) from (J).

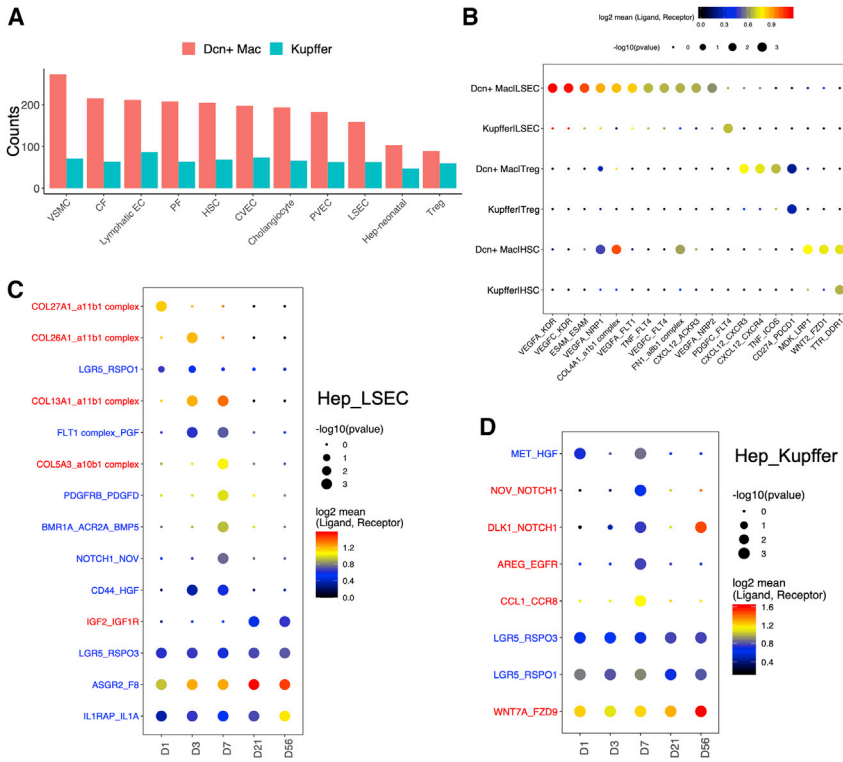


Figure 7. Predicted hepatic cell-cell interactions

(A) Bar plot comparing numbers of significant ligand-receptor interactions between indicated cell types and *Dcn*⁺ Mac or Kupffer cells.

(B) Dot plot of selected ligand-receptor interactions between *Dcn*⁺ Mac and indicated cell types (*Dcn*⁺ Mac|LSEC, *Dcn*⁺ Mac|Treg, and *Dcn*⁺ Mac|HSC) or between Kupffer and LSEC (Kupffer|LSEC, Kupffer|Treg, and Kupffer|HSC). For example, “molecule-A_moleculeB in cell C|cell D” indicates the putative interaction between molecule A expressed by cell type C and molecule B expressed by cell type D. p values are indicated by circle sizes, and the means of the average expression levels of interacting ligand and receptor are indicated by color.

(C and D) Dot plot of selected ligand-receptor interactions between hepatocytes and LSECs (C) or Kupffer cells (D). Interacting pairs in red indicate ligands expressed by hepatocytes; interacting pairs in blue indicate ligands expressed by LSECs or Kupffer cells.

interactions between hepatocytes and all other NPCs (Figure S9B). For almost all cell types closely interacting with hepatocytes, the most active cross-talk occurred at D7, as compared with other time points. Some interaction pairs, including PDGFRB-PDGFD between hepatocytes and LSECs (Figure 7C) and NOV-NOTCH1 between hepatocyte and Kupffer cells (Figure 7D), were only identified at D7. Therefore, this scRNA-seq analysis revealed a critical time point D7 in the postnatal liver, involving numerous molecular and cellular activities and communications.

DISCUSSION

This study provides the detailed blueprint that describes step-wise changes at single-cell resolution to illustrate how a neonatal liver develops into a major metabolic organ. Trajectory analysis revealed progressive and concerted development and functional maturation of hepatocytes and LSECs in a metabolic zone construction. Complex interactions between hepatic cell types are apparently involved in coordinating developmental programs in the early stages. Remarkably, we identified a group of macrophages at D7 that exhibits a hybrid phenotype of macrophages and endothelial cells. Intercellular interaction analysis suggests a putative role of *Dcn*⁺ Mac in regulation of sinusoidal vascularization and Treg cells.

Hepatocytes displayed high levels of heterogeneity in the early developmental stages after birth. In the neonatal liver, hepatocytes highly expressed hepatoblast or HCC markers, including *Afp*, *Ahsg*, and *H19*. We also identified a unique *Scd2*⁺ hepatocyte subtype at D1, whose expression was gradually replaced by *Scd1*, suggesting a specific role of *Scd2* in neonatal liver

analysis enabled us to explore the developmental trajectory based on the samples collected from multiple time points. The unbiased analysis of upstream regulators and enriched pathways predicted an establishment of liver circadian clock after birth regulated by factors, such as *Bhlhe40* (*Dec1*), and also inferred dynamic changes of several critical metabolic pathways in adaptation to dramatic environmental changes in neonatal life. A previous study measured expression of 25 selected metabolism-related genes in liver lysates using real-time PCR (Nakagaki et al., 2018). We found that most of these pathways changed in an increasing trend, although few metabolic pathways peaked in newborns and decreased later. Due to a sudden hypoglycemia environment occurring at birth due to disruption of glucose supply from mothers, neonates had two strategies to overcome this crisis, by enhancing gluconeogenesis and glycogenolysis. Another mechanism is the enhanced β -oxidation to generate acetyl-CoA for synthesis of ketone bodies as energy source. We also detected dynamic changes in fatty-acid metabolism in the ER and mitochondria, which requires further investigation.

The scRNA-seq data analysis suggests that the metabolic zonation profile is not fully developed before weaning at D21. Although immunostaining showed an E-cadherin⁺ layer of hepatocytes surrounding PV at D21 (Figure 2N), combined transcriptome profiling and zonation prediction demonstrated that the D21 hepatocytes had not shared different metabolic labors yet as in the adult liver. Furthermore, the periportal area matured later than the pericentral area, as suggested by zonation prediction (Figure 2M) and pseudotemporal analysis (Figure 3C). Pseudotemporal analysis with integrated embryonic (Lotto et al., 2020) and postnatal datasets revealed similar developmental

pattern for endothelial cells (Figures 4C–4E). As reported earlier, the development of the vascular system in portal triad is initiated soon after birth (Swartley et al., 2016). Consistent with previous data (Planas-Paz et al., 2016; Rocha et al., 2015), we identified RSPO1/3-LGR5 interactions between LSECs and hepatocytes and between Kupffer cells and hepatocytes (Figures 7C and 7D), suggesting an important role in controlling hepatocyte zonation. Other ligands expressed by LSECs or Kupffer cells, including PDGF, HGF, PGF, and BMP, might also regulate hepatocyte proliferation and zone remodeling at the early stage.

In previous experiments, we observed highly similar transcriptomic profiles between liver tumors and 1-month-old young liver tissues (Wang et al., 2019). The shared gene expression patterns between actively developing liver tissue and liver tumor will be instrumental for search of new biomarkers in HCC initiation and progression. Indeed, a rare hepatocyte subpopulation highly expressing *Scd2* was enriched only in the D1 liver. Elevated expression of *Scd2* was also detected in Myc-induced HCC (Chen et al., 2021), accompanied by significantly reduced *Scd1* expression, showing a similar pattern as D1 hepatocytes. Several upstream regulators identified in developmental trajectories showed correlation with HCC patients' survival. A premature circadian clock program was observed in neonatal liver, and circadian deregulations drive spontaneous HCC development (Hanley et al., 2021; Kettner et al., 2016).

Starting around E13–E14, hematopoietic cells migrate from the embryonic liver to thymus, spleen, and bone marrow (Crawford et al., 2010). We did observe the complete processes of erythrocyte, neutrophil, and B cell lineage differentiation from progenitor cells in the D1, D3, and D7 datasets (Figure 5A). Consistent with previous bulk RNA-seq data of the liver (Gunewardena et al., 2015; Li et al., 2009), D7 is a critical time point, at which we identified highly enriched *Dcn*⁺ Mac and Treg cells and observed active interactions between hepatocytes and other cell types. *Dcn*⁺ Mac is a previously unrecognized cell subtype with a hybrid phenotype of macrophages and endothelial cells. The coexpression of LYVE-1, ERG, and F4/80 in one single cell visualized under a confocal microscope indicates that *Dcn*⁺ Mac is not a doublet mistakenly detected by scRNA-seq or FACS. The *Dcn*⁺ Mac cells were likely derived from Kupffer cells and acquired endothelial cell markers and engaged in interaction with LSEC, HSC, fibroblast, mesothelial, and Treg cells. Our data also suggest that CXCL12-GRK6-CXCR4 signaling between *Dcn*⁺ Mac and Treg cells may promote Treg-cell recruitment and activity.

Although this work fills in a gap of knowledge on the postnatal stage of development between embryonic and adult livers at single-cell resolution, several key results may provide fresh views on previously unappreciated high levels of hepatocyte heterogeneity in the neonatal and postnatal livers, the progressive construction of metabolic zones in hepatocytes from pericentral to periportal regions, and the concerted development of hepatocytes and neighboring endothelial cells, HSC, and Kupffer cells. Further dissection of the newly identified *Dcn*⁺ Mac cell functions and their interactions with other hepatic cell types may contribute to better understanding of temporal development of the unique immune-tolerant environment in the liver.

Limitations of the study

For scRNA-seq analysis, we isolated single cells from the neonatal livers from D1 to D7 without perfusion because it was unnecessary and not feasible, although a two-step perfusion method was used for isolation of single cells from D21 and D56 livers. The two different isolation methods may affect proportions of hepatic and hematopoietic cells captured in the analysis. The conclusions inferred by bioinformatics methods, such as trajectory analysis, RNA velocity, and zonation prediction, require further validation by experimental and functional investigations.

STAR★METHODS

Detailed methods are provided in the online version of this paper and include the following:

- KEY RESOURCES TABLE
- RESOURCE AVAILABILITY
 - Lead contact
 - Materials availability
 - Data and code availability
- EXPERIMENTAL MODEL AND SUBJECT DETAILS
 - Mice
- METHOD DETAILS
 - Liver cell isolation for scRNA-seq
 - Single cell library construction and sequencing
 - scRNA-seq data pre-processing, dimensionality reduction and clustering
 - Zonation profile prediction of hepatocytes
 - Trajectory analysis
 - RNA velocity analysis
 - Monocle
 - Monocle 3
 - Force-directed graph analysis
 - Gene regulatory network analysis
 - Single cell pathway enrichment
 - Cell-cell interaction analysis
 - TCGA survival analysis
 - Immunostaining and FISH
 - Flow cytometry analysis
 - qRT-PCR
 - Statistical analysis

SUPPLEMENTAL INFORMATION

Supplemental information can be found online at <https://doi.org/10.1016/j.devcel.2022.01.004>.

ACKNOWLEDGMENTS

We thank our lab members for helpful discussion. Single-cell RNA-seq was conducted at the IGM Genomics Core at UCSD funded by NIH SIG grant (#S10 OD026929). This work was supported by NIH grants (R01DK128320, R01CA236074, and R01CA239629) to G.S.F. J.L. was supported by a postdoc fellowship from ILCA and a pinnacle award from AASLD. Funding source for microscopy core: NINDS P30NS047101

AUTHOR CONTRIBUTIONS

Conceptualization: Y.L. and G.-S.F.; methodology: Y.L., K.Z., and G.-S.F.; software: Y.L.; investigation: Y.L., K.K., J.L., and B.X.; data analysis and

interpretation: Y.L., X.S., K.Z., and G.-S.F.; writing – original draft: Y.L. and G.-S.F.; writing, reviewing, and editing: Y.L., K.K., J.L., X.S., K.Z., and G.-S.F.; supervision and funding acquisition: G.-S.F.

DECLARATION OF INTERESTS

The authors declare no competing interests.

Received: April 28, 2021

Revised: November 10, 2021

Accepted: January 5, 2022

Published: February 7, 2022

REFERENCES

- Aibar, S., González-Blas, C.B., Moerman, T., Huynh-Thu, V.A., Imrichova, H., Hulselmans, G., Rambow, F., Marine, J.C., Geurts, P., Aerts, J., et al. (2017). SCENIC: single-cell regulatory network inference and clustering. *Nat. Methods* **14**, 1083–1086. <https://doi.org/10.1038/nmeth.4463>.
- Alvarez, M., Rahmani, E., Jew, B., Garske, K.M., Miao, Z., Benhammou, J.N., Ye, C.J., Pisegna, J.R., Pietiläinen, K.H., Halperin, E., and Pajukanta, P. (2020). Enhancing droplet-based single-nucleus RNA-seq resolution using the semi-supervised machine learning classifier DIEM. *Sci. Rep.* **10**, 11019. <https://doi.org/10.1038/s41598-020-67513-5>.
- Asahina, K., Zhou, B., Pu, W.T., and Tsukamoto, H. (2011). Septum transversum-derived mesothelium gives rise to hepatic stellate cells and perivascular mesenchymal cells in developing mouse liver. *Hepatology* **53**, 983–995. <https://doi.org/10.1002/hep.24119>.
- Bahar Halpern, K., Caspi, I., Lemze, D., Levy, M., Landen, S., Elinav, E., Ulitsky, I., and Itzhkovitz, S. (2015). Nuclear retention of mRNA in mammalian tissues. *Cell Rep* **13**, 2653–2662. <https://doi.org/10.1016/j.celrep.2015.11.036>.
- Balog, S., Li, Y., Ogawa, T., Miki, T., Saito, T., French, S.W., and Asahina, K. (2020). Development of capsular fibrosis beneath the liver surface in humans and mice. *Hepatology* **71**, 291–305. <https://doi.org/10.1002/hep.30809>.
- Bergen, V., Lange, M., Peidli, S., Wolf, F.A., and Theis, F.J. (2020). Generalizing RNA velocity to transient cell states through dynamical modeling. *Nat. Biotechnol.* **38**, 1408–1414. <https://doi.org/10.1038/s41587-020-0591-3>.
- Bjerregaard, M.D., Jurlander, J., Klausen, P., Borregaard, N., and Cowland, J.B. (2003). The in vivo profile of transcription factors during neutrophil differentiation in human bone marrow. *Blood* **101**, 4322–4332. <https://doi.org/10.1182/blood-2002-03-0835>.
- Böhme, H.J., Sparmann, G., and Hofmann, E. (1983). Biochemistry of liver development in the perinatal period. *Experientia* **39**, 473–483. <https://doi.org/10.1007/bf01965164>.
- Borregaard, N., and Cowland, J.B. (1997). Granules of the human neutrophilic polymorphonuclear leukocyte. *Blood* **89**, 3503–3521.
- Braeuning, A., Ittrich, C., Köhle, C., Haifinger, S., Bonin, M., Buchmann, A., and Schwarz, M. (2006). Differential gene expression in periportal and perivenous mouse hepatocytes. *FEBS J* **273**, 5051–5061. <https://doi.org/10.1111/j.1742-4658.2006.05503.x>.
- Busillo, J.M., Armando, S., Sengupta, R., Meucci, O., Bouvier, M., and Benovic, J.L. (2010). Site-specific phosphorylation of CXCR4 is dynamically regulated by multiple kinases and results in differential modulation of CXCR4 signaling. *J. Biol. Chem.* **285**, 7805–7817. <https://doi.org/10.1074/jbc.M109.091173>.
- Butler, A., Hoffman, P., Smibert, P., Papalexi, E., and Satija, R. (2018). Integrating single-cell transcriptomic data across different conditions, technologies, and species. *Nat. Biotechnol.* **36**, 411–420. <https://doi.org/10.1038/nbt.4096>.
- Cao, J., Spielmann, M., Qiu, X., Huang, X., Ibrahim, D.M., Hill, A.J., Zhang, F., Mundlos, S., Christiansen, L., Steemers, F.J., et al. (2019). The single-cell transcriptional landscape of mammalian organogenesis. *Nature* **566**, 496–502. <https://doi.org/10.1038/s41586-019-0969-x>.
- Chakarov, S., Lim, H.Y., Tan, L., Lim, S.Y., See, P., Lum, J., Zhang, X.M., Foo, S., Nakamizo, S., Duan, K., et al. (2019). Two distinct interstitial macrophage populations coexist across tissues in specific subtissular niches. *Science* **363**. <https://doi.org/10.1126/science.aau0964>.
- Chen, W.S., Liang, Y., Zong, M., Liu, J.J., Kaneko, K., Hanley, K.L., Zhang, K., and Feng, G.S. (2021). Single-cell transcriptomics reveals opposing roles of Shp2 in Myc-driven liver tumor cells and microenvironment. *Cell Rep* **37**, 109974. <https://doi.org/10.1016/j.celrep.2021.109974>.
- Crawford, L.W., Foley, J.F., and Elmore, S.A. (2010). Histology atlas of the developing mouse hepatobiliary system with emphasis on embryonic days 9.5–18.5. *Toxicol. Pathol.* **38**, 872–906. <https://doi.org/10.1177/0192623310374329>.
- Dobie, R., Wilson-Kanamori, J.R., Henderson, B.E.P., Smith, J.R., Matchett, K.P., Portman, J.R., Wallenborg, K., Picelli, S., Zagorska, A., Pendem, S.V., et al. (2019). Single-cell transcriptomics uncovers zonation of function in the mesenchyme during liver fibrosis. *Cell Rep* **29**, 1832–1847.e8. <https://doi.org/10.1016/j.celrep.2019.10.024>.
- Doi, Y., Tamura, S., Nammo, T., Fukui, K., Kiso, S., and Nagafuchi, A. (2007). Development of complementary expression patterns of E- and N-cadherin in the mouse liver. *Hepatol. Res.* **37**, 230–237. <https://doi.org/10.1111/j.1872-034X.2007.00028.x>.
- Drapkin, R., Le Roy, G., Cho, H., Akoulitchev, S., and Reinberg, D. (1996). Human cyclin-dependent kinase-activating kinase exists in three distinct complexes. *Proc. Natl. Acad. Sci. USA* **93**, 6488–6493. <https://doi.org/10.1073/pnas.93.13.6488>.
- Efremova, M., Vento-Tormo, M., Teichmann, S.A., and Vento-Tormo, R. (2020). CellPhoneDB: inferring cell-cell communication from combined expression of multi-subunit ligand-receptor complexes. *Nat. Protoc.* **15**, 1484–1506. <https://doi.org/10.1038/s41596-020-0292-x>.
- Elliott, S., and Sinclair, A.M. (2012). The effect of erythropoietin on normal and neoplastic cells. *Biologics* **6**, 163–189. <https://doi.org/10.2147/BTT.S32281>.
- Géraud, C., Schledzewski, K., Demory, A., Klein, D., Kaus, M., Peyre, F., Sticht, C., Evdokimov, K., Lu, S., Schmieder, A., and Goerd, S. (2010). Liver sinusoidal endothelium: a microenvironment-dependent differentiation program in rat including the novel junctional protein liver endothelial differentiation-associated protein-1. *Hepatology* **52**, 313–326. <https://doi.org/10.1002/hep.23618>.
- Ginhoux, F., and Guillems, M. (2016). Tissue-resident macrophage ontogeny and homeostasis. *Immunity* **44**, 439–449. <https://doi.org/10.1016/j.immuni.2016.02.024>.
- Gola, A., Dorrington, M.G., Speranza, E., Sala, C., Shih, R.M., Radtke, A.J., Wong, H.S., Baptista, A.P., Hernandez, J.M., Castellani, G., et al. (2021). Commensal-driven immune zonation of the liver promotes host defence. *Nature* **589**, 131–136. <https://doi.org/10.1038/s41586-020-2977-2>.
- Gordillo, M., Evans, T., and Gouon-Evans, V. (2015). Orchestrating liver development. *Development* **142**, 2094–2108. <https://doi.org/10.1242/dev.114215>.
- Gunewardena, S.S., Yoo, B., Peng, L., Lu, H., Zhong, X., Klaassen, C.D., and Cui, J.Y. (2015). Deciphering the developmental dynamics of the mouse liver transcriptome. *PLoS One* **10**, e0141220. <https://doi.org/10.1371/journal.pone.0141220>.
- Halpern, K.B., Shenhav, R., Massalha, H., Toth, B., Egozi, A., Massasa, E.E., Medgalia, C., David, E., Giladi, A., Moor, A.E., et al. (2018). Paired-cell sequencing enables spatial gene expression mapping of liver endothelial cells. *Nat. Biotechnol.* **36**, 962–970. <https://doi.org/10.1038/nbt.4231>.
- Halpern, K.B., Shenhav, R., Matcovitch-Natan, O., Toth, B., Lemze, D., Golan, M., Massasa, E.E., Baydatch, S., Landen, S., Moor, A.E., et al. (2017). Single-cell spatial reconstruction reveals global division of labour in the mammalian liver. *Nature* **542**, 352–356. <https://doi.org/10.1038/nature21065>.
- Hanley, K.L., Liang, Y., Wang, G., Lin, X., Yang, M., Karin, M., Fu, W., and Feng, G.S. (2021). Concurrent disruption of Ras/MAPK and NF- κ B pathways induces circadian deregulation and hepatocarcinogenesis. *Mol. Cancer Res.* <https://doi.org/10.1158/1541-7786.MCR-21-0479>.
- Honma, S., Kawamoto, T., Takagi, Y., Fujimoto, K., Sato, F., Noshiro, M., Kato, Y., and Honma, K. (2002). Dec1 and Dec2 are regulators of the mammalian molecular clock. *Nature* **419**, 841–844. <https://doi.org/10.1038/nature01123>.

- Iozzo, R.V. (1999). The biology of the small leucine-rich proteoglycans. Functional network of interactive proteins. *J. Biol. Chem.* 274, 18843–18846. <https://doi.org/10.1074/jbc.274.27.18843>.
- Iwaisako, K., Jiang, C., Zhang, M., Cong, M., Moore-Morris, T.J., Park, T.J., Liu, X., Xu, J., Wang, P., Paik, Y.H., et al. (2014). Origin of myofibroblasts in the fibrotic liver in mice. *Proc. Natl. Acad. Sci. USA* 111, E3297–E3305. <https://doi.org/10.1073/pnas.1400062111>.
- Jungermann, K., and Kietzmann, T. (1996). Zonation of parenchymal and non-parenchymal metabolism in liver. *Annu. Rev. Nutr.* 16, 179–203. <https://doi.org/10.1146/annurev.nu.16.070196.001143>.
- Juriscic, G., Iolyeva, M., Proulx, S.T., Halin, C., and Detmar, M. (2010). Thymus cell antigen 1 (Thy1, CD90) is expressed by lymphatic vessels and mediates cell adhesion to lymphatic endothelium. *Exp. Cell Res.* 316, 2982–2992. <https://doi.org/10.1016/j.yexcr.2010.06.013>.
- Kanehisa, M., and Goto, S. (2000). KEGG: kyoto encyclopedia of genes and genomes. *Nucleic Acids Res* 28, 27–30. <https://doi.org/10.1093/nar/28.1.27>.
- Kettner, N.M., Voicu, H., Finegold, M.J., Coarfa, C., Sreekumar, A., Putluri, N., Katchy, C.A., Lee, C., Moore, D.D., and Fu, L. (2016). Circadian homeostasis of liver metabolism suppresses hepatocarcinogenesis. *Cancer Cell* 30, 909–924. <https://doi.org/10.1016/j.ccell.2016.10.007>.
- La Manno, G., Soldatov, R., Zeisel, A., Braun, E., Hochgerner, H., Petukhov, V., Lidschreiber, K., Kastrioti, M.E., Lönnerberg, P., Furlan, A., et al. (2018). RNA velocity of single cells. *Nature* 560, 494–498. <https://doi.org/10.1038/s41586-018-0414-6>.
- Li, M., Zhao, W., Wang, Y., Jin, L., Jin, G., Sun, X., Wang, W., Wang, K., Xu, X., Hao, J., et al. (2020). A wave of Foxp3⁺ regulatory T cell accumulation in the neonatal liver plays unique roles in maintaining self-tolerance. *Cell. Mol. Immunol.* 17, 507–518. <https://doi.org/10.1038/s41423-019-0246-9>.
- Li, T., Huang, J., Jiang, Y., Zeng, Y., He, F., Zhang, M.Q., Han, Z., and Zhang, X. (2009). Multi-stage analysis of gene expression and transcription regulation in C57/B6 mouse liver development. *Genomics* 93, 235–242. <https://doi.org/10.1016/j.ygeno.2008.10.006>.
- Li, Y., Wang, J., and Asahina, K. (2013). Mesothelial cells give rise to hepatic stellate cells and myofibroblasts via mesothelial-mesenchymal transition in liver injury. *Proc. Natl. Acad. Sci. USA* 110, 2324–2329. <https://doi.org/10.1073/pnas.1214136110>.
- Lim, H.Y., Lim, S.Y., Tan, C.K., Thiam, C.H., Goh, C.C., Carbajo, D., Chew, S.H.S., See, P., Chakarov, S., Wang, X.N., et al. (2018). Hyaluronan receptor LYVE-1-Expressing macrophages maintain arterial tone through hyaluronan-mediated regulation of smooth muscle cell collagen. *Immunity* 49, 1191. <https://doi.org/10.1016/j.immuni.2018.12.009>.
- Lindgren, I.M., Drake, R.R., Chattergoon, N.N., and Thornburg, K.L. (2019). Down-regulation of MEIS1 promotes the maturation of oxidative phosphorylation in perinatal cardiomyocytes. *FASEB J* 33, 7417–7426. <https://doi.org/10.1096/fj.201801330RR>.
- Lotto, J., Drissler, S., Cullum, R., Wei, W., Setty, M., Bell, E.M., Boutet, S.C., Nowotschin, S., Kuo, Y.Y., Garg, V., et al. (2020). Single-cell transcriptomics reveals early emergence of liver parenchymal and non-parenchymal cell lineages. *Cell* 183, 702–716.e14. <https://doi.org/10.1016/j.cell.2020.09.012>.
- Mishima, Y., Miyagi, S., Saraya, A., Negishi, M., Endoh, M., Endo, T.A., Toyoda, T., Shinga, J., Katsumoto, T., Chiba, T., et al. (2011). The Hbo1-Brd1/Brpf2 complex is responsible for global acetylation of H3K14 and required for fetal liver erythropoiesis. *Blood* 118, 2443–2453. <https://doi.org/10.1182/blood-2011-01-331892>.
- Mishima, Y., Wang, C., Miyagi, S., Saraya, A., Hosokawa, H., Mochizuki-Kashio, M., Nakajima-Takagi, Y., Koide, S., Negishi, M., Sashida, G., et al. (2014). Histone acetylation mediated by Brd1 is crucial for Cd8 gene activation during early thymocyte development. *Nat. Commun.* 5, 5872. <https://doi.org/10.1038/ncomms6872>.
- Miyajima, A., Tanaka, M., and Itoh, T. (2014). Stem/progenitor cells in liver development, homeostasis, regeneration, and reprogramming. *Cell Stem Cell* 14, 561–574. <https://doi.org/10.1016/j.stem.2014.04.010>.
- Miyazaki, M., Dobrzyn, A., Elias, P.M., and Ntambi, J.M. (2005). Stearoyl-CoA desaturase-2 gene expression is required for lipid synthesis during early skin and liver development. *Proc. Natl. Acad. Sci. USA* 102, 12501–12506. <https://doi.org/10.1073/pnas.0503132102>.
- Miyazaki, M., Jacobson, M.J., Man, W.C., Cohen, P., Asilmaz, E., Friedman, J.M., and Ntambi, J.M. (2003). Identification and characterization of murine SCD4, a novel heart-specific stearyl-CoA desaturase isoform regulated by leptin and dietary factors. *J. Biol. Chem.* 278, 33904–33911. <https://doi.org/10.1074/jbc.M304724200>.
- Mu, T., Xu, L., Zhong, Y., Liu, X., Zhao, Z., Huang, C., Lan, X., Lufeif, C., Zhou, Y., Su, Y., et al. (2020). Embryonic liver developmental trajectory revealed by single-cell RNA sequencing in the Foxa2(eGFP) mouse. *Commun. Biol.* 3, 642. <https://doi.org/10.1038/s42003-020-01364-8>.
- Nakagaki, B.N., Mafra, K., de Carvalho, É., Lopes, M.E., Carvalho-Gontijo, R., de Castro-Oliveira, H.M., Campolina-Silva, G.H., de Miranda, C.D.M., Antunes, M.M., Silva, A.C.C., et al. (2018). Immune and metabolic shifts during neonatal development reprogram liver identity and function. *J. Hepatol.* 69, 1294–1307. <https://doi.org/10.1016/j.jhep.2018.08.018>.
- Nowotschin, S., Setty, M., Kuo, Y.Y., Liu, V., Garg, V., Sharma, R., Simon, C.S., Saiz, N., Gardner, R., Boutet, S.C., et al. (2019). The emergent landscape of the mouse gut endoderm at single-cell resolution. *Nature* 569, 361–367. <https://doi.org/10.1038/s41586-019-1127-1>.
- Ochsner, S.A., Strick-Marchand, H., Qiu, Q., Venable, S., Dean, A., Wilde, M., Weiss, M.C., and Darlington, G.J. (2007). Transcriptional profiling of bipotential embryonic liver cells to identify liver progenitor cell surface markers. *Stem Cells* 25, 2476–2487. <https://doi.org/10.1634/stemcells.2007-0101>.
- Pijuan-Sala, B., Griffiths, J.A., Guibentif, C., Hiscock, T.W., Jawaid, W., Calero-Nieto, F.J., Mulas, C., Ibarra-Soria, X., Tyser, R.C.V., Ho, D.L.L., et al. (2019). A single-cell molecular map of mouse gastrulation and early organogenesis. *Nature* 566, 490–495. <https://doi.org/10.1038/s41586-019-0933-9>.
- Planas-Paz, L., Orsini, V., Boulter, L., Calabrese, D., Pikiokle, M., Nigsch, F., Xie, Y., Roma, G., Donovan, A., Marti, P., et al. (2016). The RSP0-LGR4/5-ZNRF3/RNF43 module controls liver zonation and size. *Nat. Cell Biol.* 18, 467–479. <https://doi.org/10.1038/ncb3337>.
- Popescu, D.M., Botting, R.A., Stephenson, E., Green, K., Webb, S., Jardine, L., Calderbank, E.F., Polanski, K., Goh, I., Efremova, M., et al. (2019). Decoding human fetal liver haematopoiesis. *Nature* 574, 365–371. <https://doi.org/10.1038/s41586-019-1652-y>.
- Qiu, Q., Hernandez, J.C., Dean, A.M., Rao, P.H., and Darlington, G.J. (2011). CD24-positive cells from normal adult mouse liver are hepatocyte progenitor cells. *Stem Cells Dev* 20, 2177–2188. <https://doi.org/10.1089/scd.2010.0352>.
- Qiu, X., Mao, Q., Tang, Y., Wang, L., Chawla, R., Pliner, H.A., and Trapnell, C. (2017). Reversed graph embedding resolves complex single-cell trajectories. *Nat. Methods* 14, 979–982. <https://doi.org/10.1038/nmeth.4402>.
- Rocha, A.S., Vidal, V., Mertz, M., Kendall, T.J., Charlet, A., Okamoto, H., and Schedl, A. (2015). The angiocrine factor Rspondin3 is a key determinant of liver zonation. *Cell Rep* 13, 1757–1764. <https://doi.org/10.1016/j.celrep.2015.10.049>.
- Rugh, R. (1990). *The mouse: Its Reproduction and Development* (Oxford University Press).
- Sasaki, K., and Matsumura, G. (1986). Haemopoietic cells of yolk sac and liver in the mouse embryo: a light and electron microscopical study. *J. Anat.* 148, 87–97.
- Sato, F., Kawamoto, T., Fujimoto, K., Noshiro, M., Honda, K.K., Honma, S., Honma, K., and Kato, Y. (2004). Functional analysis of the basic helix-loop-helix transcription factor DEC1 in circadian regulation. Interaction with BMAL1. *Eur. J. Biochem.* 271, 4409–4419. <https://doi.org/10.1111/j.1432-1033.2004.04379.x>.
- Spear, B.T., Jin, L., Ramasamy, S., and Dobierzewska, A. (2006). Transcriptional control in the mammalian liver: liver development, perinatal repression, and zonal gene regulation. *Cell. Mol. Life Sci.* 63, 2922–2938. <https://doi.org/10.1007/s00018-006-6258-5>.
- Stuart, T., Butler, A., Hoffman, P., Hafemeister, C., Papalexi, E., Mauck, W.M., Hao, Y., Stoeckius, M., Smibert, P., and Satija, R. (2019). Comprehensive

- integration of single-cell data. *Cell* 177, 1888–1902.e21. <https://doi.org/10.1016/j.cell.2019.05.031>.
- Su, X., Shi, Y., Zou, X., Lu, Z.N., Xie, G., Yang, J.Y.H., Wu, C.C., Cui, X.F., He, K.Y., Luo, Q., et al. (2017). Single-cell RNA-Seq analysis reveals dynamic trajectories during mouse liver development. *BMC Genomics* 18, 946. <https://doi.org/10.1186/s12864-017-4342-x>.
- Subramanian, A., Tamayo, P., Mootha, V.K., Mukherjee, S., Ebert, B.L., Gillette, M.A., Paulovich, A., Pomeroy, S.L., Golub, T.R., Lander, E.S., and Mesirov, J.P. (2005). Gene set enrichment analysis: a knowledge-based approach for interpreting genome-wide expression profiles. *Proc. Natl. Acad. Sci. USA* 102, 15545–15550. <https://doi.org/10.1073/pnas.0506580102>.
- Swartley, O.M., Foley, J.F., Livingston, D.P., Cullen, J.M., and Elmore, S.A. (2016). Histology atlas of the developing mouse hepatobiliary hemolymphatic vascular system with emphasis on embryonic days 11.5–18.5 and early post-natal development. *Toxicol. Pathol.* 44, 705–725. <https://doi.org/10.1177/0192623316630836>.
- Torre, C., Perret, C., and Colnot, S. (2010). Molecular determinants of liver zonation. *Prog. Mol. Biol. Transl. Sci.* 97, 127–150. <https://doi.org/10.1016/B978-0-12-385233-5.00005-2>.
- Trapnell, C., Cacchiarelli, D., Grimsby, J., Pokharel, P., Li, S., Morse, M., Lennon, N.J., Livak, K.J., Mikkelsen, T.S., and Rinn, J.L. (2014). The dynamics and regulators of cell fate decisions are revealed by pseudotemporal ordering of single cells. *Nat. Biotechnol.* 32, 381–386. <https://doi.org/10.1038/nbt.2859>.
- Wang, G., Luo, X., Liang, Y., Kaneko, K., Li, H., Fu, X.D., and Feng, G.S. (2019). A tumorigenic index for quantitative analysis of liver cancer initiation and progression. *Proc. Natl. Acad. Sci. USA* 116, 26873–26880. <https://doi.org/10.1073/pnas.1911193116>.
- Whitfield, M.L., George, L.K., Grant, G.D., and Perou, C.M. (2006). Common markers of proliferation. *Nat. Rev. Cancer* 6, 99–106. <https://doi.org/10.1038/nrc1802>.
- Yang, L., Wang, W.H., Qiu, W.L., Guo, Z., Bi, E., and Xu, C.R. (2017). A single-cell transcriptomic analysis reveals precise pathways and regulatory mechanisms underlying hepatoblast differentiation. *Hepatology* 66, 1387–1401. <https://doi.org/10.1002/hep.29353>.
- Zaret, K.S. (2002). Regulatory phases of early liver development: paradigms of organogenesis. *Nat. Rev. Genet.* 3, 499–512. <https://doi.org/10.1038/nrg837>.
- Zhao, R., and Duncan, S.A. (2005). Embryonic development of the liver. *Hepatology* 41, 956–967. <https://doi.org/10.1002/hep.20691>.

STAR★METHODS

KEY RESOURCES TABLE

| REAGENT or RESOURCE | SOURCE | IDENTIFIER |
|--|-----------------|-----------------------------------|
| Immunostaining antibodies | | |
| Rabbit monoclonal anti-E-Cadherin | Santa Cruz | Cat# sc-7870; RRID: AB_2076666 |
| Rabbit polyclonal Anti-CYP2E1 | Santa Cruz | Cat# sc-133491; RRID: AB_10608738 |
| Rat monoclonal anti-F4/80 | eBioscience | Cat# 14-4801-82; RRID: AB_467558 |
| Rabbit monoclonal anti-ERG | Abcam | Cat# ab92513; RRID: AB_2630401 |
| Goat polyclonal anti-LYVE-1 | R&D Systems | Cat# AF2125, RRID: AB_2297188 |
| FACS antibodies | | |
| LIVE/DEAD Fixable Aqua Stain | ThermoFisher | Cat# L34957 |
| Rat monoclonal anti-CD16/CD32 | eBioscience | Cat# 14-0161-85; RRID: AB_467134 |
| Rat monoclonal anti-CD45, PerCP-Cy5.5 | BioLegend | Cat# 147706; RRID: AB_2563538 |
| Rat monoclonal anti-B220, BV711 | BioLegend | Cat# 103255; RRID: AB_2563491 |
| Rat monoclonal anti-CD146, PE-Cy7 | BioLegend | Cat# 134714; RRID: AB_2563109 |
| Rat monoclonal anti-F4/80, Alexa Fluor 594 | BioLegend | Cat# 123140; RRID: AB_2563241 |
| Chemicals, peptides, and recombinant proteins | | |
| Hanks' Balanced Salt solution (HBSS) | Gibco | Cat# 14185-052; 14065-056 |
| EGTA | Sigma-Aldrich | Cat# E3889 |
| HEPES | HyClone | Cat# SH30237.01 |
| DNase I | Roche | Cat# 10104159001 |
| Collagenase H | Roche | Cat# 11074032001 |
| ACK Lysing Buffer | Gibco | Cat# A10492-01 |
| Percoll | Cytiva | Cat# 17-0891-02 |
| Dulbecco's Modified Eagle's Medium (DMEM) | gibco | Cat# 10313-021 |
| Fetal bovine serum (FBS) | HyClone | Cat# SH30070.03 |
| Tissue-Tek O.C.T. Compound | Sakura | Cat# 4583 |
| Paraformaldehyde (PFA) | Sigma-Aldrich | Cat# P6148 |
| Triton X-100 | Sigma-Aldrich | Cat# X100 |
| Bovine Serum Albumin | Spectrum | Cat# A3611 |
| VECTASHIELD with DAPI | Avantor | Cat# H-1200 |
| Anti-Fade Fluorescence Mounting Medium - Aqueous, Fluoroshield | Abcam | Cat# ab104135 |
| Critical commercial assays | | |
| gentleMACS Dissociator | Miltenyi | Cat# 130-093-235 |
| gentleMACS C Tubes | Miltenyi | Cat# 130-093-237 |
| MidiMACS separator | Miltenyi | Cat# 130-042-302 |
| LS columns | Miltenyi | Cat# 130-042-401 |
| Dead cell removal kit | Miltenyi | Cat# 130-090-101 |
| Chromium Single Cell 3' Reagent Kits (v2 Chemistry) | Miltenyi | Cat# CG00052 |
| Oligonucleotides | | |
| Scd1 – qPCR FWD | Eton Bioscience | GCGATACACTCTGGTGCTCA |
| Scd1 – qPCR REV | Eton Bioscience | CCCAGGGAAACCAGGATATT |
| Scd2 – qPCR FWD | Eton Bioscience | GCTCTCGGGAGAACATCTTG |
| Scd2 – qPCR REV | Eton Bioscience | CAGCCCTGGACACTCTCTTC |
| F4/80 – qPCR FWD | Eton Bioscience | CTTTGGCTATGGGCTCCAGTC |

(Continued on next page)

Continued

| REAGENT or RESOURCE | SOURCE | IDENTIFIER |
|---|---|---|
| <i>F4/80</i> – qPCR REV | Eton Bioscience | GCAAGGAGGACAGAGTTTATCGTG |
| <i>Clec4f</i> – qPCR FWD | Eton Bioscience | CTTCGGGAAGCAACAACACTC |
| <i>Clec4f</i> – qPCR REV | Eton Bioscience | CAAGCAACTGCACCAGAGAAC |
| <i>Lyve1</i> – qPCR FWD | Eton Bioscience | GAAAACCTCTGTTGCGGGTGT |
| <i>Lyve1</i> – qPCR REV | Eton Bioscience | CCTCCAGCCAAAAGTTCAAA |
| <i>Alb</i> – qPCR FWD | Eton Bioscience | GCAGATGACAGGGCGGAACCTG |
| <i>Alb</i> – qPCR REV | Eton Bioscience | CAGCAGCAATGGCAGGCAGAT |
| <i>Gapdh</i> – qPCR FWD | Eton Bioscience | CGACTTCAACAGCAACTCCCCTTCC |
| <i>Gapdh</i> – qPCR REV | Eton Bioscience | TGGGTGGTCCAGGGTTTCTTACTCCT |
| Deposited data | | |
| Adult hepatocytes (processed scRNA-seq data) | (Halpern et al., 2017) | Supplementary tables |
| E7.5, E8.75, E9.5 and E10.5 endothelial cell (processed scRNA-seq data) | Single Cell Portal (Lotto et al., 2020) | SCP1022 |
| Software and algorithms | | |
| FlowJo v10.6.2 | BD | https://www.flowjo.com |
| GraphPad Prism 9 | GraphPad | https://www.graphpad.com/scientific-software/prism/ |
| ImageJ/FIJI | ImageJ | https://imagej.net/Fiji |
| Cellranger v3.0.2 | 10x Genomics | https://www.10xgenomics.com/ |
| R | The R Foundation | https://www.r-project.org/ |
| Seurat v3.0.2 | Butler et al., 2018; Stuart et al., 2019 | https://github.com/satijalab/seurat |
| Monocle | Cao et al., 2019; Qiu et al., 2017; Trapnell et al., 2014 | http://cole-trapnell-lab.github.io/monocle-release/ |
| SCENIC v1.1.2.2 | Aibar et al., 2017 | https://github.com/aertslab/SCENIC |
| RNA Velocity | La Manno et al., 2018 | http://velocyto.org/velocyto.py/index.html |
| scVelo | Bergen et al., 2020 | https://scvelo.readthedocs.io/ |
| CellphoneDB | Efremova et al., 2020 | https://github.com/Teichlab/cellphonedb |
| Other | | |
| HCR FISH probe: <i>Neat1</i> | Molecular Instruments | GenBank: NR_131212.1 |
| HCR FISH probe: <i>Malat1</i> | Molecular Instruments | GenBank: NR_002847.2 |

RESOURCE AVAILABILITY

Lead contact

Further information and requests for resources and reagents should be directed to and will be fulfilled by the Lead Contact, Gen-Sheng Feng (gfheng@health.ucsd.edu).

Materials availability

This study did not generate new unique reagents.

Data and code availability

The accession number for the raw data and processed data reported in this paper is GSE171993.

EXPERIMENTAL MODEL AND SUBJECT DETAILS

Mice

All animals used in this study were in C57BL/6J background. The animal protocol (S09108) was approved by the IACUC at the University of California San Diego.

METHOD DETAILS

Liver cell isolation for scRNA-seq

For neonatal samples (D1, D3 and D7), 4 male mice were included in each time point. Decapitation was used for neonate sacrifice because they are resistance to hypoxia at this age. First, fetal livers were removed from the body, cut into small pieces and rinsed using Ca^{2+} -free HBSS to reduce blood. Next, liver pellets were transferred into HBSS buffer with collagenase H and DNase I, further dissociated with gentleMACS program *m_liver_03* and then incubated at 37°C for 30 minutes. After incubation, the additional gentleMACS program *m_liver_04* was used for more complete dissociation. Liver was passed through a 100 μm cell strainer. Cells were then centrifuged at 50 g for 3 minutes, in order to separate hepatocytes (in pellets) from non-parenchymal cells, NPCs (in suspension). In non-parenchymal cell suspension, ACK buffer was added to lyse red blood cells. Hepatocytes and NPCs were further washed with PBS separately, resuspended in DMEM with 10% FBS, counted with hemocytometer and mixed by original ratios of cell numbers.

For D21 and D56 samples, 2 male mice were included for each time point. Mice were first sacrificed using CO_2 . Liver was perfused using a 2-step method with Ca^{2+} -free HBSS buffer and then with collagenase H in HBSS buffer containing Ca^{2+} , gently minced and passed through a 100 μm cell strainer. Cells were centrifuged at 50 g for 3 min, in order to separate hepatocytes (in pellets) from NPCs (in suspension). To remove dead cells and debris, the pelleted hepatocytes were resuspended in 45% Percoll and centrifuged at 50 g for 10 min, without brake. Meanwhile, the ACK buffer and Dead Cell Removal Kit were used to lyse red blood cells and eliminate dead cells in non-parenchymal cells. Hepatocytes and NPCs were further washed with PBS separately, resuspended in DMEM with 10% FBS and counted with hemocytometer.

Liver single cell preparations were made within the same four-hour period of a day for collection of samples at all five time points.

Single cell library construction and sequencing

The isolated single cells were immediately loaded onto 10x Chromium Controller, and then partitioned into nanoliter-scale Gel Beads-In-Emulsion (GEMs). Cells in GEMs were lysed, and RNAs released from cells were immediately captured by barcoded beads in the same GEMs, followed by reverse transcription, amplification, fragmentation, adaptor ligation and index PCR. Libraries were constructed using Chromium Single Cell 3' Reagent Kits (V2 chemistry, 10x Genomics). Sequencing was performed on Illumina HiSeq 4000 at IGM Genomics Center, UCSD, with the following read length: Read 1, 26 bp, including 16 bp cell barcode and 12 bp unique molecular identifier (UMI); Read 2, 98 bp transcript insert; i7 sample index, 8 bp.

scRNA-seq data pre-processing, dimensionality reduction and clustering

Sequenced reads were aligned to mouse reference genome GRCm38 using Cell Ranger package (v3.0.2). All libraries were then aggregated for batch effect correction and sequencing depth normalization. An expression matrix including all cells from D1 to D56 livers was generated, with each row representing a gene and each column representing a cell, and then loaded into the R package, Seurat. Next, low quality cells and genes were filtered for downstream analysis. In brief, genes expressed in less than 3 cells were removed; cells failed to meet following criteria were removed: 1) the number of genes detected in each cell should be more than 200 but less than 6500; 2) the UMIs of mitochondrial genes should be less than 10% of total UMI. A total of 52834 cells and 24057 genes passed the filter. After filtering, the raw expression matrix was normalized by the total expression, multiplied by scale factor 10,000, and log transformed. Next, we regressed on total numbers of UMIs per cell as well as mitochondrial gene percentages. The z-scored residuals calculated by normalization and scaling were stored for downstream analysis. We then performed dimensionality reduction and unsupervised clustering using Seurat functions. In brief, PCA was performed first, and 75 PCs were loaded for UMAP and tSNE dimensionality reduction. To find clusters, the same PCs were imported into FindClusters, a SNN graph-based clustering algorithm, with resolution = 3.0. Next, the Wilcoxon Rank Sum test was performed to identify markers (FDR < 0.05) in each cluster. Cell types were then assigned based on these markers manually.

Further, to find subpopulations in hepatocyte, endothelial cells, mesenchymal cells, NK cells, T cells and Kupffer cells, cells from corresponding groups were segregated and re-analyzed for higher resolution.

For combined analysis of embryonic (Lotto et al., 2020) and fetal (this work) endothelial cells, an additional dataset integration using Seurat was performed to remove batch effect.

Zonation profile prediction of hepatocytes

We predicted spatial layers (zonation) of hepatocytes using linear regression method. The training dataset was downloaded from previously published work (Halpern et al., 2017), with processed expression matrix and zonation information for each cell. We normalized, scaled and integrated this dataset with our hepatocyte subpopulations to remove batch effect. Next, the Wilcoxon Rank Sum test was performed to identify markers (FDR < 0.05) in each layer. We combined markers for 9 layers to make a zonation signature with 210 genes in total. With zonation signature gene set, the linear model was trained using original dataset (Halpern et al., 2017) and then used to predict layer for single hepatocyte in this study. The predicted layer was then normalized from 1 to 9, representing spatial distribution of hepatocytes from pericentral to periportal area.

Trajectory analysis

We performed trajectory analysis using different methods listed below, depending on different situations and purposes.

RNA velocity analysis

As described in original publication (La Manno et al., 2018), this algorithm was designed based on a simple model for transcriptional dynamics, in which the RNA velocity was estimated from spliced and un-spliced mRNA, and then used to predict the future state of individual cells. We first generated loom files of spliced and un-spliced reads counts from 10x samples using *velocity* *run10x* pipeline. We then visualized RNA velocity on specified tSNE or UMAP embedding. For gene of interest, we also plotted (1) spliced or (2) un-spliced counts on the same embedding, (3) phase portraits against steady-state (un-spliced levels on y-axis above steady-state represented gene of interest being induced, while un-spliced levels below steady-state represented being repressed), and (4) residual levels u , with positive (red) and negative (blue) values indicating induced and repressed, respectively, embedded onto the same dimensionality reduction.

Monocle

This method was used to perform trajectory analysis and calculate pseudotime for a relatively small group of cells. In brief, we selected differentially expressed genes between different time points as ordering genes and applied DDRTree, which learned the structure of dataset manifold as developmental trajectory and ordered cells onto that manifold with a calculated pseudotime starting from a given root cell. Next, we selected genes significantly changed as a function of pseudotime along trajectory. In brief, for each gene, the expression level was fitted with natural spline (*sm.ns*) to describe the smooth change of this gene along trajectory. The smooth values were then employed to fit a negative binomial model via *vglm()* function from VGAM package. This was the full model. Next, to test for significance, a chi-square ratio test was performed to compare this full model against null model. The whole process was wrapped in *differentialGeneTest* function in *monocle*. We adapted this method here and also for analysis described below. Finally, we made heatmap with significantly changed genes, clustered them by pseudotemporal expression pattern and then performed pathway enrichment analysis with gene sets from *Msigdb* v7.0 (Subramanian et al., 2005).

Monocle 3

For a much larger dataset, we performed trajectory analysis for integrated embryonic and fetal endothelial cells using *monocle 3* with UMAP visualization for a better performance.

Force-directed graph analysis

This method was performed to visualize connections between immature hematopoietic cells and their progenitor cells, with pseudotime calculated (not shown). The code was adapted from published work on fetal liver hematopoiesis (Popescu et al., 2019).

Gene regulatory network analysis

SCENIC (Single Cell Regulatory Network Inference and Clustering) was performed to identify upstream regulators important for hepatocyte, LSEC and Kupffer cell development individually. With segregated raw expression matrix for cell type of interest, we further filtered for genes expressed at least with a count of 3 in 1% of all cells and genes found in *RcisTarget*'s mouse databases (mm9-500bp-upstream-7species.mc9nr.feather, mm9-tss-centered-10kb-7species.mc9nr.feather). Next, the filtered expression matrix was normalized as $\log_2(\text{exprMat} + 1)$. SCENIC was then performed to identify and score regulons (TFs) based on the expression of their regulated target genes. With regulon scores, we adopted differential expression function from *Monocle* to test for TFs with significantly changed activities as a function of pseudotime. We fitted regulon score with gamma distribution instead and also performed chi-square ratio test for significance. A similar heatmap was plotted for TF activities using regulon scores. Also, for a TF of interest, we fitted natural spline to its scaled expression values (Expression) and regulon scores (Activity) and plotted the smooth change of said TF along pseudotime, which was stretched from 0 to 100.

Single cell pathway enrichment

We collected metabolism-related pathways from Kyoto Encyclopedia of Genes and Genomes (KEGG) and *Msigdb*. To find metabolic pathways significantly changed during postnatal development, we first calculated enrichment score for individual cell i of each gene set j . The score was defined as follows:

$$S_{ij} = n_j / \sum_{k=1}^{n_j} \text{rank}_{ik},$$

where n_j represented the length of gene set j ; rank_{ik} represented the rank of cell i ordered by expression levels of gene k (in gene set j) over all cells included in this analysis. Next, for each gene set j , we ordered cells along trajectory and tested if S_{ij} changed significantly as a function of pseudotime. The statistical test method was also adapted from *monocle* as described above. We fitted gene set enrichment scores with gamma distribution and performed chi-square ratio test for significance. Similarly, we plotted smooth scores after fitting the natural spline.

Cell-cell interaction analysis

We performed *CellPhoneDB* with our dataset to identify important ligand-receptor interactions. All cell types were included for the analysis at each time point. The genes encoding ligands and receptors were kept only if they were expressed by at least 10% of cells. The significance of an interaction was calculated by permutation test with iterations = 1000.

TCGA survival analysis

The TCGA dataset of HCC was downloaded from TCGA-LIHC project, including processed results of RNA-sequencing and clinical information for 371 patients. For each gene of interest, all samples were divided into three groups based on gene expression levels: Low (patients with expression levels lower than 33.3% percentile); High (patients with expression levels higher than 66.7% percentile); Mid (other patients). Survival analysis was performed using survival and survminer R package, including the Low and High groups divided based on gene of interest.

Immunostaining and FISH

To prepare fresh frozen tissue sections, all liver tissues were collected at indicated time points and were immediately embedded Tissue-Tek O.C.T compound (Sakura) and stored at -80°C . Fresh frozen tissue sections were fixed by cold acetone overnight, followed by cold 4% PFA overnight. After primary and secondary antibody incubation, fresh frozen tissue sections were mounted with VECTASHIELD mounting medium with DAPI or Anti-Fade Fluorescence Mounting Medium (for confocal microscope). For single-cell resolution, we checked slides under Leica SP8 Confocal with Lightning Deconvolution at microscopy core, UCSD. Quantification on the fluorescence intensity across the zonation was performed using imageJ. HCR FISH (Molecular Instruments) was performed according to manufacturer's instruction. Mean fluorescence intensity for individual nucleus was analyzed with ImageJ, and Pearson's correlation analysis was performed with GraphPad Prism.

Flow cytometry analysis

Non-parenchymal cells were isolated from liver as described above (see [liver cell isolation for scRNA-seq](#)). Cells were first stained for LIVE/DEAD fixable Aqua, anti-CD16/CD32 for Fc blocking, and then panel antibodies. Cells were fixed using 1% PFA in PBS overnight at 4°C , resuspended in PBS, and analyzed on BD LSRFortessa X-20 Cell Analyzer at UCSD Human Embryonic Stem Cell Core facility at Sanford Consortium for Regenerative Medicine. Data were then analyzed using FlowJo 10.6.2.

qRT-PCR

RNAs were extracted from different cell types at indicated time points using RNeasy kit (Qiagen, cat #73304) following manufacturer's instruction. Real-time PCR was conducted to check mRNA levels of genes at indicated time points. *gapdh* was used as a housekeeping control. The primers used in this study were listed in [key resources table](#).

Statistical analysis

The statistical analysis was performed using R or GraphPad Prism 9 (for FACS analysis only). The details of test and significance are specified in figure legends.